Petroleum 11 (2025) 290–307

Contents lists available at ScienceDirect

Petroleum

journal homepage: www.keaipublishing.com/en/journals/petlm

Full Length Article

Characteristics and genesis analysis of middle and lower Ordovician dolomite in the southern margin of the Ordos Basin, China

Xinyi Tang [a], Zijing Li [b], Hong Fang [b], Yang Li [b, *], Zongyang Dai [c], Tian Li [d], Peng Lai [b]

[a] Chengdu Kingray Information Technology Co. Ltd., Chengdu, 610000, China
[b] Liaohe Oilfield of CNPC, Panjin, 124010, China
[c] School of Geoscience and Technology, Southwest Petroleum University, Chengdu, 610500, China
[d] Sichuan Earthquake Agency, Chengdu, 610041, China

ARTICLE INFO

Article history:
Received 22 July 2024
Received in revised form
10 April 2025
Accepted 14 May 2025

Keywords:
Ordos basin
Ordovician system
Geochemical analysis
Dolomite characteristics
Dolomite genesis

ABSTRACT

The Middle-Lower Ordovician formations in the southern margin of the Ordos Basin host multiple sets of dolomites, which readily form high-quality reservoirs with promising exploration prospects. Understanding the geochemical characteristics and analyzing the genesis of these dolomites in this region is crucial. Based on drilling, logging, core observation, and thin section identification, representative dolomite samples from the Xiweikou, Jueshangou, and Caojiagou profiles were selected for comprehensive geochemical analysis. Combined with the petrological characteristics and cathodoluminescence features of the dolomites, their characteristics and genesis were analyzed. The results indicate that the average $^{87}Sr/^{86}Sr$ ratio of 11 dolomite samples in this area is 0.710842. The rare earth element distribution pattern shows an enrichment of light rare earth elements (LREE) and a depletion of heavy rare earth elements (HREE). The micritic and finely crystalline dolomite crystals are euhedral to subhedral, with low ordering, high Na, K, Sr, and low Fe, Mn content. Under cathodoluminescence, they emit rose-red to dark-red light, indicating a product of penecontemporaneous dolomitization. The sandy crystalline dolomites (fine, medium, and coarse crystalline) generally have anhedral to subhedral crystal forms, high ordering, low Na, K, Sr, and high Fe, Mn content. Under cathodoluminescence, they emit dark-red or no light, indicating a product of burial diagenesis.

1. Introduction

Dolomite reservoirs account for approximately one-quarter of global oil and gas fields and hold significant exploration value [1–8]. Dolomite was named by French geologist Dolomieu in 1791 following its discovery in the Dolomites of northern Italy [9] and has remained a focus of research for scholars worldwide. Mineralogically, dolomite often contains more than 50% dolomite minerals, with micritic to finely crystalline crystals (0.005~0.25 mm) and coarsely crystalline particles (0.25~2 mm) described as “sucrosic dolomite” due to their sugar-like texture [3,7,10–15]. Under the microscope, dolomite commonly exhibits cloudy cores and bright rims, along with banded structures [3,7,10–15].

The genesis of dolomite has long been a key research topic in geology, with multiple dolomitization models proposed—such as sabkha dolomitization, reflux seepage dolomitization, burial dolomitization, microbial dolomitization, hydrothermal dolomitization, and mixed-water dolomitization [7,16–24]. Among these, sabkha dolomitization is often associated with highly evaporative, arid settings [19], typically forming micritic to finely crystalline dolomites accompanied by gypsum nodules, laminations, halite pseudomorphs, birdseye structures, and fenestrae [25–28]. Reflux seepage dolomitization occurs when evaporative brines migrate downward, leading to various textural outcomes from finely crystalline to grainy dolomite [5,16,25,27,29–32]. Burial dolomitization commonly arises in deeper settings and may involve overprinting or readjusting earlier dolomite, facilitated by elevated temperatures, pressures, and Mg/Ca ratios [3,7,18,22,33].

A growing body of research illustrates the diverse origins of dolomite in various basins. For instance, Marheni et al. [34] concluded that Late Jurassic Arabian strata in Abu Dhabi primarily

* Corresponding author.
E-mail address: 7891235@qq.com (Y. Li).
Peer review under the responsibility of Editorial Office of Petroleum.

https://doi.org/10.1016/j.petlm.2025.05.003

underwent sabkha pumping and seepage-reflux dolomitization, while Ali [35] reported that the dolomicrosparite and dolosparite in the Pila Spi Formation (Late Eocene) of northern Iraq possibly formed via seepage-reflux under shallow-burial conditions. Bai et al. [23] identified microbial and sabkha dolomitization in Ordovician reservoirs of the Tarim Basin, whereas Jiang et al. [36] highlighted reflux seepage and burial dolomitization in the Lower Cambrian Longwangmiao Formation. Moreover, Li et al. [37] attributed Middle Permian Maokou Formation dolomites in eastern Sichuan Basin to a combination of reflux and hydrothermal dolomitization.

In the present study area, the Lower Paleozoic strata exhibit low exploration maturity but high potential, with three principal reservoir types—weathering crust karst reservoirs, intercrystalline dolomite reservoirs, and reef-shoal pore reservoirs—mostly distributed along karst slopes, ancient uplift flanks, and platform margin slope facies belts. Based on Permian (Taiyuan and Shanxi formations) and Middle-Upper Ordovician source rock relationships, two major pre-Carboniferous petroleum systems (weathering crust system and interior system) have been delineated, both showing significant exploration prospects. However, limited understanding of the Lower Paleozoic petroleum systems has hindered effective exploration strategies and the selection of drilling targets. To address these issues, this study performs a systematic petrological and geochemical investigation of the Middle-Lower Ordovician dolomite reservoirs. By integrating cathodoluminescence observations and analyses of carbon, oxygen, and strontium isotopes, electron probe microanalysis, trace elements, and rare earth elements, we aim to refine the genetic models of dolomite formation. The findings will provide a geological basis for clarifying the developmental mechanisms of high-quality dolomite reservoirs, thereby enhancing reservoir prediction and guiding future exploration.

2. Geological settings and dolomite distribution

The study area is situated on the southern margin of the Ordos Basin, extending from Qingyang City in Gansu Province to Linyou County in Shaanxi Province longitudinally, and from Long County in Gansu Province to Tongchuan City in Shaanxi Province latitudinally, encompassing parts of both provinces and comprising three structural units: the Yishan Slope, the Weibei Uplift, and the Tianhuan Depression [38,39]. The Ordovician system within this region is well-developed, consisting primarily of the Lower Ordovician Yeli Formation, Liangjiashan Formation, and Majiagou Formation, the Middle Ordovician Majiagou Formation, and the Upper Ordovician Pingliang Formation and Beiguoshan Formation. Stratigraphically, the Ordovician overlies the Cambrian conformably and is unconformably overlain by the Carboniferous. Although there are slight variations in the subdivision and nomenclature of the Ordovician across different parts of the basin, the stratigraphic boundaries of the Yeli-Liangjiashan Formation, Majiagou Formation, and Pingliang-Beiguoshan Formation remain largely consistent [25,31,38,40–43] (Fig. 1).

Within these strata, dolomite predominantly develops in the supratidal and intertidal zones of a restricted platform environment[44–47], where intense seawater evaporation can lead to the coexistence of dolomite and gypsum, particularly in the Yeli-Liangjiashan Formation where dolomite crystals tend to be larger compared to the typically smaller crystals found in the Majiagou Formation. The dolomites in the study area encompass a variety of lithological types, including crystalline dolomite, granular dolomite, muddy dolomite, calcareous dolomite, gypsum-bearing dolomite, and algal dolomite, reflecting diverse depositional environments and complex diagenetic processes. Crystalline dolomites are widely distributed across multiple formations, exhibiting a range of crystal sizes from micritic to finely crystalline and sandy crystalline forms; micritic and finely crystalline dolomites, commonly observed in wells such as L22, L29, XT1, LT1, CH2, and outcrop profiles like Xiweikou, Tiewadian, and Yucheshen, see Fig. 2(a)-(e), typically display grayish-white to dark gray colors and form in low-energy tidal flat environments with mud contents in intercrystalline micropores or microfractures usually not exceeding 8%, thereby limiting further crystal growth. Fine crystalline dolomite is characterized by subhedral to anhedral granular mosaic structures with mud content up to 10%, while coarse crystalline dolomite often exhibits cloudy core–bright rim structures and diagonal features under the microscope, as Fig. 2(b) and (d). Sandy crystalline dolomite includes fine, medium, coarse, and very coarse crystalline varieties (Fig. 2(f)-(j)), with fine crystalline grains ranging from 0.15 mm to 0.2 mm often mixed with less than 10% medium and coarse crystalline dolomite, predominantly exhibiting euhedral or subhedral forms, and notable for well-developed primary intercrystalline pores or dissolution pores that contribute to high porosity and the formation of high-quality reservoirs. Additionally, cloudy core–bright rim and banded structures are commonly observed, especially near intercrystalline, dissolution, or fracture pores with larger grains, see Fig. 2(f), (k), (l). Medium crystalline dolomite grains, generally ranging from 0.3 mm to 0.4 mm and often mixed with minor amounts of fine and coarse crystalline dolomite, tend to form aggregate structures that diminish the euhedral quality of the dolomite and primarily display subhedral granular mosaic structures, with well-developed dissolution pores and cloudy core–bright rim and banded structures prevalent, and intercrystalline pores frequently filled with micritic calcite, asphalt, etc. Coarse to very coarse crystalline dolomite, with grain sizes between 0.5 mm and 1.8 mm, is exclusively found in the Yeli-Liangjiashan Formation, predominantly exhibiting subhedral granular mosaic structures, cloudy core–bright rim, banded, and aggregate structures under the microscope, indicative of formation in medium to deep burial diagenetic environments, see Fig. 2(g), (h), (j). Calcareous dolomite, a transitional carbonate rock type where dolomite content exceeds that of calcite, features micritic calcite and dolomite crystals varying widely in size from micritic to finely or medium crystalline forms, often displaying uneven dolomitization characterized by a “floating” distribution of rhombohedral dolomite crystals under the microscope and “leopard spot” textures in outcrop profiles, see Fig. 2(m), (n). Granular dolomite, predominantly observed in wells CT3, L28, LT1, and outcrop profiles such as Xiweikou, Tiewadian, and Taoqupo, originates from granular limestone (mainly micritic brecciated limestone) that undergoes intense dolomitization during subsequent burial diagenesis, thereby preserving much of the original granular structure as Fig. 2(o), (p). The intergranular cementation consists of micritic or finely crystalline dolomite around particles, with crystal sizes increasing towards pore centers, transitioning from fine to medium and then to coarse crystalline dolomite, and dark organic matter or mud is often present between grains, with residual structures commonly observed, indicating formation in high-energy conditions such as platform margin shoals. Muddy dolomite, typically developing in the supratidal zones of a restricted platform and classified based on mud content into muddy dolomite and mudstone dolomite, can also be referred to as muddy micritic dolomite, muddy finely crystalline dolomite, or muddy sandy crystalline dolomite due to varying dolomite crystal sizes. Widely distributed in the study area, muddy dolomite is characterized by high mud content and darker colors, primarily ranging from dark gray to gray-black, with laminar structures and relatively poor porosity development, see Fig. 2(q), (r). Gypsum-bearing dolomite generally develops in evaporative-restricted platforms of the Yeli-

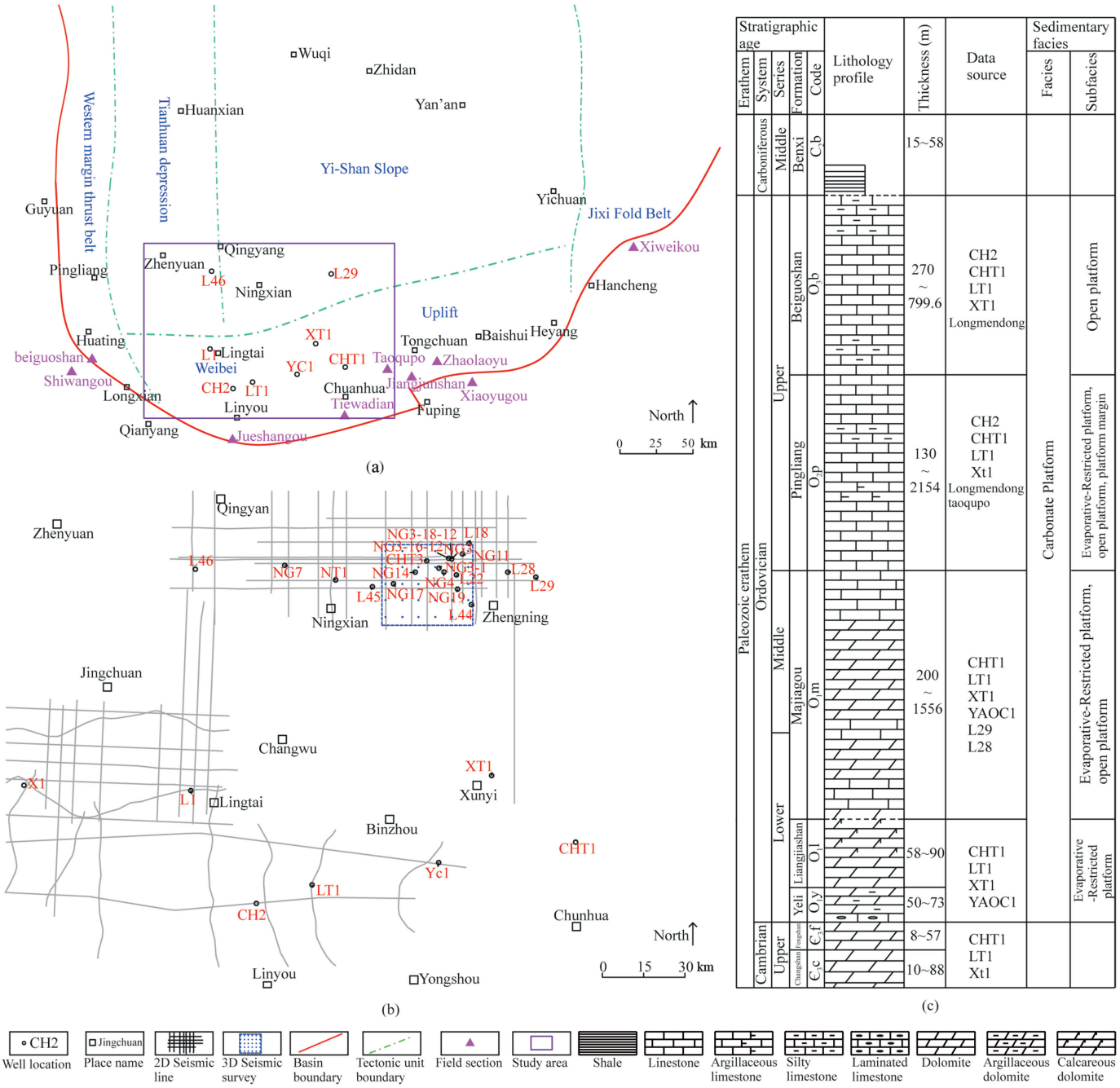

Fig. 1. Comprehensive geological background map of the study area. (a) structural map of the southern margin of the Ordos Basin and the location of the study area; (b) seismic survey lines, grid network, and well location map; (c) comprehensive stratigraphic column of the Ordovician in the southern margin of the Ordos Basin.

Liangjiashan Formation, specifically within the Ma 1 to Ma 3 members and Ma 5 member, and is observable in wells LT1, XT1, CHT1, and YAOC1, while algal dolomite typically forms in the southern part of the study area within the Ma 5 and Ma 6 members and the Pingliang-Beiguoshan Formation, exemplified by gray algal dolomite present in the core section from 4181.0 m to 4184.02 m in the Ma 6 member of well CH2, see Fig. 2(s), (t). Through the detailed descriptions above, the geological background and the diverse characteristics of dolomites in the study area are comprehensively presented, providing a solid foundation for subsequent methodological approaches and result analyses.

3. Methods and results

3.1. Sample preparation and testing methods

Representative dolomite samples were selected from the Xiweikou, Jueshangu, and Caojiagou profiles for comprehensive geochemical analysis, including carbon and oxygen isotopes, strontium isotopes, major elements (electron probe), trace elements, and rare earth elements. These analyses were combined with the petrological characteristics and cathodoluminescence features of the dolomites to comprehensively study the genesis of

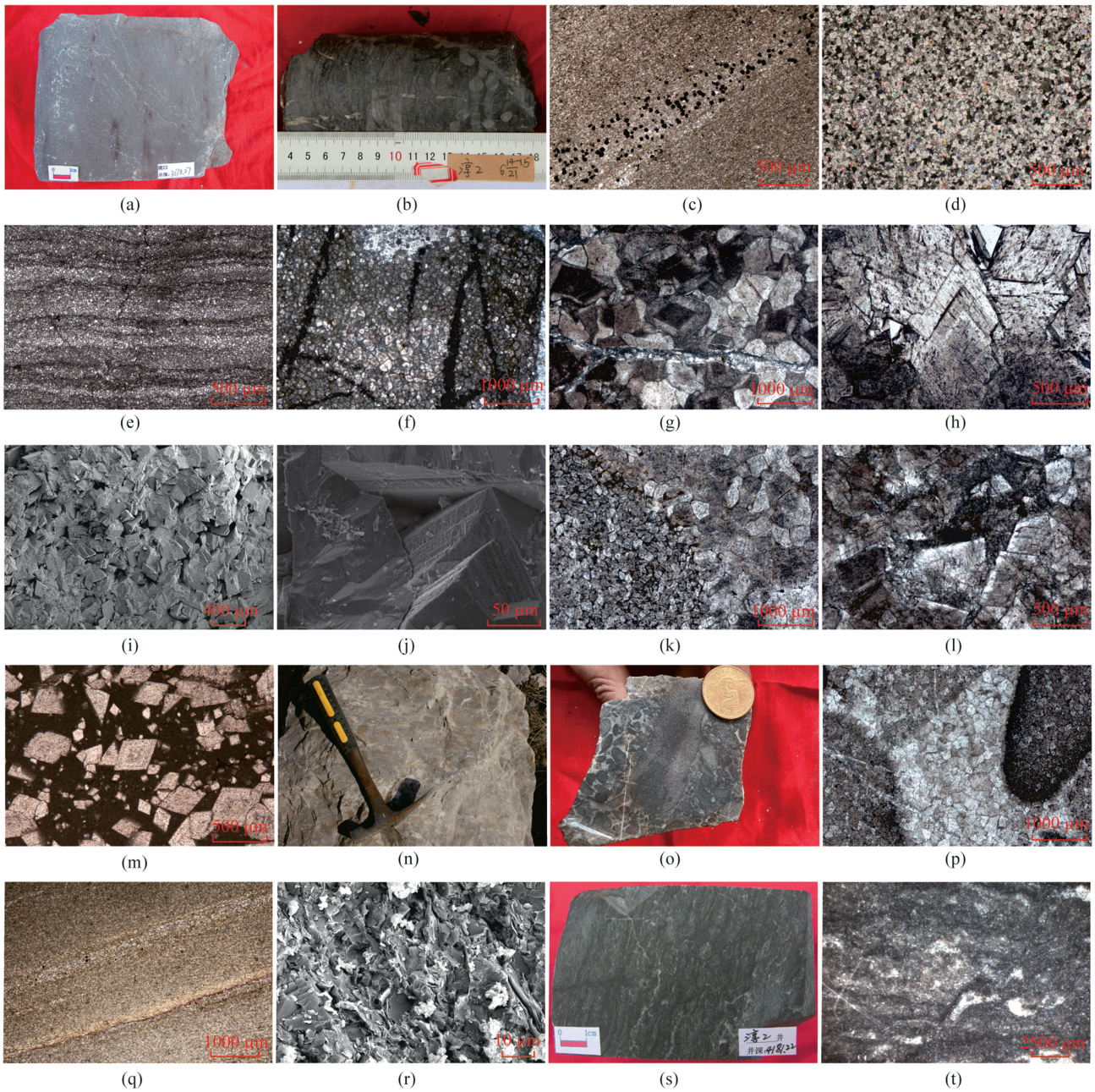

Fig. 2. Macroscopic and microscopic characteristics of dolomites. (a). grayish-white micritic dolomite, homogeneous massive, Well L22, Ma 2 Member, 3678.27 m; (b). dark gray finely crystalline dolomite with flocculent gypsum, Well CH2, Ma 5 Member, 4183.35 m; (c). micritic dolomite with laminar distribution of pyrite, Well L29, Ma 3 Member, 3922.9 m, plane-polarized light (−); (d) coarse finely crystalline dolomite, evenly distributed subhedral-anhedral grains, Well L22, Ma 2 Member, 3676.05 m, plane-polarized light (+); (e). micritic-finely crystalline dolomite with algal laminae, Jueshangu, Ma 6 member, plane-polarized light (−); (f) grayish finely crystalline dolomite with cloudy core-bright rim structure, intercrystalline and intercrystalline dissolution pores filled with calcite, slight dedolomitization, Tiewadian, Ma 6 Member, 4181.35 m; (g) coarse to very coarse crystalline dolomite with good euhedral quality, cloudy core-bright rim structure, fractures filled with siliceous material and pyrite, Caojiagou, Yeli Formation, thin section (−); (h) medium to coarse crystalline dolomite with banded and cloudy core-bright rim structures, Xiweikou, Yeli-Liangjiashan Formation, thin section (−); (i) medium crystalline dolomite with good euhedral quality and developed intercrystalline pores, Well XT1, Ma 6 member, 3301.55 m, scanning electron microscope (SEM); (j) medium to coarse crystalline dolomite with banded dolomite crystals, Xiweikou, Yeli-Liangjiashan Formation, SEM; (k) fine to medium crystalline dolomite, Xiweikou, Yeli-Liangjiashan Formation, plane-polarized light (−); (l) fine to medium crystalline dolomite with banded coarse crystalline dolomite growing along dissolution pores, Caojiagou, Yeli-Liangjiashan Formation, plane-polarized light (−); (m) calcareous medium crystalline dolomite with rhombohedral floating dolomite distribution, Tiewadian, Ma 5 member, plane-polarized light (−); (n) calcareous dolomite with "leopard spot" pattern, Heiniugou, Ma 6 member; (o) brecciated dolomite with well-rounded breccia clasts and developed fractures, Xiweikou, Yeli-Liangjiashan Formation; (p) brecciated fine crystalline dolomite with residual breccia structure, Xiweikou, Yeli-Liangjiashan Formation, thin section (−); (q) muddy dolomite with laminar structures and interlaminar fractures, Well L28, Ma 3 Member, 3861.61 m, cast thin section (−); (r) muddy dolomite with dolomite, clay minerals, and micropores, Well L28, Ma 3 member, 3861.61 m, SEM; (s) gray massive algal dolomite with developed fractures, Well CH2, Ma 5 member, 4181.22 m; (t) algal dolomite with developed intercrystalline pores, Well CH2, Ma 5 member, 4181.5 m, plane-polarized light (−).

the dolomites. The selected samples were required to be as fresh as possible, with minimal weathering. The primary strata studied were the Yeli-Liangjiashan Formation and the Majiagou Formation. The dolomite ordering, cathodoluminescence, and electron microprobe analyses were conducted at the State Key Laboratory of Oil and Gas Reservoir Geology and Exploitation at Southwest Petroleum University. Carbon and oxygen isotopes, as well as strontium isotopes, were tested at Beijing Createch Testing Technology Co., Ltd., while trace element measurements were performed at Sichuan Origin & Microspectrum Co., Ltd. The testing equipment used in all analyses was of high precision, and the resulting data fully met the requirements for analysis.

The ordering degree of dolomite was determined using X-ray diffraction (XRD) analysis. Before testing, the samples were ground using an agate mortar and sieved through a 200-mesh sieve. The data were obtained using an X'Pert PRO X-ray diffractometer, with testing temperatures ranging from 25 °C to 30 °C and humidity ≤70% RH, following the SY/T 5163-1995 standard.

For carbon and oxygen isotopes, and strontium isotopes, the samples were similarly ground and sieved. Carbon and oxygen isotopes were analyzed using a stable gas isotope ratio mass spectrometer (Delta Plus XP) at room temperature, following the DZT 0184.17–1997 method. Strontium isotopes were analyzed using a MC-ICP-MS (Neptune Plus), with an ambient temperature of 20 °C and humidity of 55%, following the BJKH-300.38-2016 method.

Selected rock samples were prepared into multiple thin sections (16 in total), allowing for cathodoluminescence, major, trace, and rare earth element analyses on the same thin section for more accurate results. Major and trace elements, and rare earth elements were measured using laser ablation inductively coupled plasma mass spectrometry (LA-ICP-MS).

Cathodoluminescence was measured using a CL8200 MK5 cathodoluminescence microscope, with a voltage of 18 kV, a current of 200 μA, a temperature of 20 °C, and relative humidity of 60%.

The electron probe used was a JEOL-JXA-8230, equipped with four spectrometers. Samples were coated with a uniform carbon film approximately 20 nm thick. The operating conditions were an accelerating voltage of 15 kV, an accelerating current of 10 nA, and a beam diameter of 10 μm. All data were corrected using ZAF correction. Measurement times for the characteristic peaks of elements Ca, Mg, Mn, Fe, Sr, and Ba were 10 s, with background measurement times for upper and lower peaks being half of the peak measurement time. International SPI standards used included Ca ($CaCO_3$), Mg ($(Mg,Ca)(CO_3)_2$), Mn ($CaMnSi_2O_6$), Fe (Fe_2O_3), Sr ($SrSO_4$), and Ba ($BaSO_4$).

In-situ trace element analysis of carbonate minerals using LA-ICP-MS employed an ASI Resolution LR 193 nm laser ablation system composed of an ArF 193 nm excimer laser and optical system. The ICP-MS model was iCap-TQ, operated in SQ mode. Prior to testing, ICP-MS was tuned using a line scan of NIST 612, with a spot size of 50 μm, frequency of 10 Hz, and energy of 3 J/cm^2, ensuring sensitivity and oxide production rates below 1%. During laser ablation, helium at 300 mL/min was used as the carrier gas, with 0.87 L/min argon as the nebulizer flow rate, and 5 ml/min high-purity nitrogen to adjust sensitivity. The laser spot size and frequency for this analysis were 67 μm and 8 Hz, respectively, with an energy density of 3 J/cm^2. MACS-3 was used as the external standard and ^{43}Ca as the internal standard (using data from electron probe measurements). Data processing was completed using iolite software. We implemented several measures to maintain the accuracy of LA-ICP-MS across different sample types, including calibrating with appropriate standard materials, regularly checking instrument performance, and using internal standards during analysis to correct for signal drift. To address the heterogeneity of dolomite samples, we performed thorough grinding and homogenization, and assessed sample representativeness through multi-point analyses. The results indicate that even with some heterogeneity, our LA-ICP-MS analyses can reliably reflect the overall geochemical characteristics of the samples.

3.2. Results

3.2.1. Dolomite ordering

It is generally believed that dolomites formed during the syngenetic stage have a lower degree of ordering, which increases with burial diagenesis as dolomite crystals grow larger. In this study, 11 samples were analyzed, with dolomite ordering degrees ranging from 0.571 to 1, with an average of 0.808. The ordering degree of micritic to finely crystalline dolomite ranged from 0.571 to 0.867, averaging 0.726, while that of sandy crystalline dolomite ranged from 0.667 to 1, averaging 0.848. The dolomite ordering degree of the Yeli-Liangjiashan period is generally higher than that of the Majiagou period, indicating an increase in ordering degree with longer burial time (Table 1).

3.2.2. Carbon and oxygen isotopes

According to Allan and Wiggins [10], the carbon and oxygen isotopes in seawater form the basis for the variation of these isotopes in dolomites of different origins. Allan et al. conducted a statistical analysis of dolomite carbon and oxygen isotopes from various regions and eras, finding that the stable carbon isotopes of Ordovician seawater ranged from −2.0‰ to +0.5‰, and stable oxygen isotopes ranged from −6.6‰ to −4.0‰[10]. Chen Qiang (2012) systematically studied the carbon and oxygen isotopes of Ordovician carbonates in the Ordos Basin, revealing that the $\delta^{13}C$ values ranged from −7.3‰ to 2.26‰, averaging −0.30‰, and the $\delta^{18}O$ values ranged from −13.14‰ to −1.94‰, averaging −6.38‰. In

Table 1
X-ray diffraction, dolomite ordering, carbon and oxygen isotopes, and strontium isotopes test results of dolomites.

Section	Sample ID	Strata	Lithology	Mineral content, %		Dolomite ordering	Carbon and oxygen isotopes, ‰		Strontium isotopes	
				Calcite	Dolomite		$\delta^{13}C_{V\text{-}PDB}$	$\delta^{18}O_{V\text{-}PDB}$	$^{87}Sr/^{86}Sr$	2σ(±)
Xiweikou	5–2	$O_1y\text{-}l$	Medium to coarse crystalline dolomite	0.38	98.60	0.895833	1.61	−6.87	0.711626	0.000007
Xiweikou	4–3	$O_1y\text{-}l$	Fine to medium crystalline dolomite	0.00	100.00	0.925926	2.05	−6.48	0.709925	0.000007
Xiweikou	10–3	$O_1y\text{-}l$	Medium to fine crystalline dolomite	0.00	93.52	0.666667	−0.45	−5.76	0.712533	0.000007
Xiweikou	11–1	$O_1y\text{-}l$	Fine crystalline dolomite	0.00	99.30	0.804348	−0.33	−6.53	0.710575	0.000007
Xiweikou	14–1	O_1m	Medium to coarse crystalline dolomite	0.96	95.16	0.833333	−2.62	−6.77	0.709348	0.000009
Xiweikou	15–1	O_1m	Micritic to coarse finely crystalline dolomite	0.00	76.79	0.571429	−1.91	−4.82	0.715552	0.000006
Xiweikou	35–1	O_2m	Fine crystalline dolomite	3.51	93.14	0.867925	−1.66	−5.91	0.709503	0.000008
Jueshangou	2–1	O_1m	Fine to coarse finely crystalline dolomite	19.07	73.47	0.714286	−1.28	−5.17	0.710306	0.000009
Caojiagou	07	$O_1y\text{-}l$	Coarse to very coarse crystalline dolomite	0.29	98.89	1	−1.30	−6.01	0.709746	0.000010
Caojiagou	12	$O_1y\text{-}l$	Fine to medium crystalline dolomite	1.04	98.30	0.814815	−2.31	−7.26	0.709899	0.000009
Caojiagou	15	$O_1y\text{-}l$	Fine to coarse finely crystalline dolomite	2.01	96.37	0.75	−0.85	−5.13	0.710246	0.000007

the southern margin of the basin, the Yeli-Liangjiashan Formation had an average $\delta^{13}C$ value of −0.60‰ and an average $\delta^{18}O$ value of −5.50‰, while the Majiagou Formation had an average $\delta^{13}C$ value of −0.14‰ and an average $\delta^{18}O$ value of −4.43‰ Chen, 2011.

Dolomite sample $\delta^{13}C$ values ranged from −2.62‰ to 2.05‰, averaging −0.82‰, and $\delta^{18}O$ values ranged from −7.62‰ to −4.82‰, averaging −6.06‰ (Table 1). Most data points fall within the range of Ordovician seawater values. Combining Allan's statistical distribution of $\delta^{18}O$ in high and low-temperature dolomites, it was found that only three data points fell into the high-temperature dolomite region, relating to burial dolomites. The remaining points were in the overlapping region, indicating possible high-temperature burial or low-temperature burial origins. In Fig. 3, it can be seen that the $\delta^{13}C$ values of two sandy crystalline dolomites are significantly more positive than Ordovician seawater values, likely related to dolomitization during the "biochemical gas" stage (biological fermentation), which produces ^{12}C-rich CH_4 that easily escapes, causing relative enrichment of ^{13}C in the dolomite [29,41].

In the study area, the $\delta^{13}C$ values of micritic to finely crystalline dolomites range from −2.31‰ to −0.85‰, averaging −1.43‰, and the $\delta^{18}O$ values range from −7.26‰ to −5.13‰, averaging −5.89‰. The $\delta^{13}C$ values of sandy crystalline dolomites range from −2.62‰ to 2.05‰, averaging −0.47‰, and the $\delta^{18}O$ values range from −6.87‰ to −4.82‰, averaging −6.16‰. Overall, the $\delta^{13}C$ values of micritic to finely crystalline dolomites are lower than those of sandy crystalline dolomites, while the $\delta^{18}O$ values are higher in micritic to finely crystalline dolomites compared to sandy crystalline dolomites (Fig. 3).

3.2.3. Strontium isotopes

Strontium primarily has two sources: one from ancient terrestrial silicate rocks. The weathering and erosion of these rocks produce terrigenous material that flows into seawater via rivers, providing strontium with a relatively high $^{87}Sr/^{86}Sr$ ratio, with a global average value of 0.7119. The other source is from mid-ocean ridge hydrothermal systems, which provide strontium with a relatively low $^{87}Sr/^{86}Sr$ ratio, with a global average value of 0.7035. The strontium in modern seawater is a mixture of these two sources, with an average $^{87}Sr/^{86}Sr$ value of 0.709073[3,10,48,49].

A total of 11 dolomite samples were tested for strontium isotopes. The $^{87}Sr/^{86}Sr$ values of these samples were relatively high, ranging from a minimum of 0.709348 to a maximum of 0.715552, with an average of 0.710842. The minimum values are already higher than the global average $^{87}Sr/^{86}Sr$ value of modern seawater, indicating that the strontium in the dolomites of the study area is more likely derived from the weathering and erosion of ancient terrestrial silicate rocks (Table 1).

3.2.4. Major and trace elements

Major and trace elements can provide comprehensive insights into the fluid properties or depositional environment of ancient rocks. For example, high Sr, Na, and K and low Fe and Mn indicate a relatively restricted depositional environment, whereas low Sr, Na, and K and high Fe and Mn suggest a relatively open depositional environment.

Using LA-ICP-MS, 61 sets of trace element data were measured, and 161 sets of major element data were tested using a JEOL-JXA-8230 electron probe (Tables 2 and 3). From the obtained experimental data, it can be observed that the Na_2O content of micritic to finely crystalline dolomites ranges from 0 to 6740 ppm, with an average of 720 ppm. K_2O content ranges from 0 to 3530 ppm, with an average of 520 ppm. Sr content ranges from 23.079 ppm to 445.057 ppm, with an average of 141.799 ppm. Zn content ranges from 0.349 ppm to 41.2 ppm, with an average of 8.352 ppm. Ba content ranges from 0.086 ppm to 35.525 ppm, with an average of 7.694 ppm. Fe content ranges from 278.163 ppm to 10237.084 ppm, with an average of 1882.203 ppm. Mn content ranges from 12.835 ppm to 357.357 ppm.

The Na_2O content of sandy crystalline dolomites ranges from 0 to 2160 ppm, with an average of 510 ppm. K_2O content ranges from 0 to 2780 ppm, with an average of 320 ppm. Sr content ranges from 21.761 ppm to 105.213 ppm, with an average of 64.940 ppm.

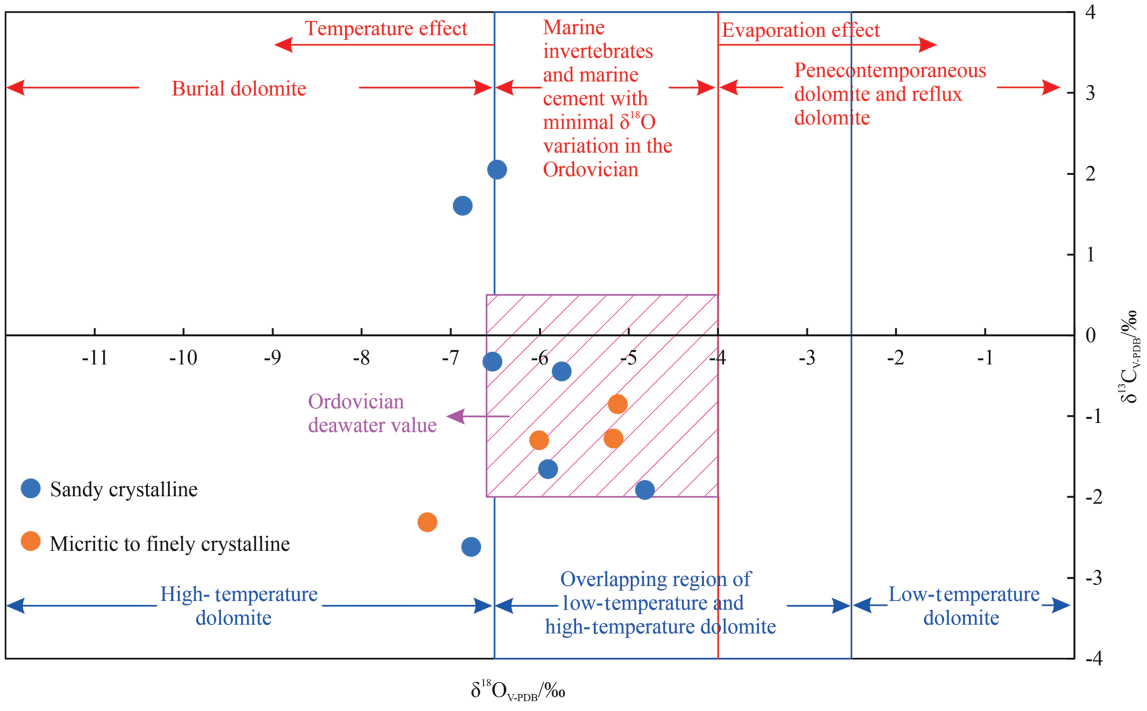

Fig. 3. Relationship Diagram of Carbon and Oxygen Isotopes in Dolomites (Base Map from Allan et al., 1993).

Table 2
Trace element content of dolomites (ppm).

Sample ID	Al	Mn	Fe	Zn	Sr	Ba	Cathodoluminescence intensity
X5-1-1	4242.523	93.939	2680.683	4.841	50.724	10.066	Dark red
X5-1-2	777.383	95.84	1891.754	3.373	63.83	1.702	Dark red
X5-2-1	296.556	532.686	3300.139	4.041	66.508	0.238	Rose red
X5-2-2	19.234	264.7	15832.647	4.736	88.295	0.166	Rose red
X5-2-3	48.596	1352.904	19394.732	3.906	32.228	0.353	Bright red
X5-2-4	27.203	223.159	7898.966	3.123	21.761	0.221	Bright red
X5-2-5	45.105	95.899	1338.972	2.815	36.778	0.29	Non-luminescent
X5-2-6	582.559	87.889	1955.723	3.331	45.148	5.25	Non-luminescent
X5-2-7	147.106	105.454	2190.181	3.053	41.376	0.524	Dark red
X4-3-1	1915.025	90.796	3629.42	4.553	42.852	13.311	Dark red
X4-3-2	2331.148	88.893	2808.008	4.13	42.134	5.959	Dark red
X4-3-3	0.817	2.205	206.289	0.359	41.172	1.081	Dark red
X4-3-4	253.098	81.676	1613.025	2.942	40.6	0.887	Dark red
X6-4-1	378.462	99.915	4555.651	3.152	54.798	1.444	Non-luminescent
X6-4-2	456.323	91.42	2136.383	2.791	68.758	1.088	Non-luminescent
X6-4-3	22.673	700.089	26355.938	13.435	89.025	1.602	Non-luminescent
X6-4-4	16.904	663.352	22680.644	5.912	57.046	0.836	Non-luminescent
X6-4-5	18.035	928.581	25785.508	5.588	56.678	1.222	Non-luminescent
X6-4-6	19.761	717.161	25018.585	4.358	51.858	1.057	Dark red
X6-4-7	18.923	501.745	26652.837	4.613	53.342	1.359	Dark red
X10-3-1	2875.58	98.637	3156.855	5.704	62.919	13.151	Dark red
X10-3-2	1662.29	115.392	7368.991	3.879	89.045	4.396	Dark red
X11-1-1	5584.687	91.086	20858.257	5.475	48.243	19.392	Pale rose red
X11-1-2	584.706	85.73	1597.754	2.947	69.282	2.074	Pale rose red
X11-1-3	132.276	100.339	998.015	2.936	53.846	0.75	Non-luminescent
X14-1-1	580.95	167.515	1410.22	4.414	77.453	4.914	Rose red
X14-1-2	2735.623	113.434	1196.303	4.538	89.78	26.448	Rose red
X14-1-3	951.689	126.132	1853.338	5.674	53.706	2.21	Rose red
X14-1-4	28.384	163.916	1260.097	2.722	68.008	0.853	Rose red
X15-1-1	19706.271	357.357	9818.778	8.119	102.406	35.525	Pale rose red
X30-1-1	10866.122	58.632	1740.222	4.044	95.379	7.218	Non-luminescent
X30-1-2	3659.677	22.281	1061.425	1.667	87.837	9.947	Non-luminescent
X30-1-3	3.208	12.835	341.316	0.349	141.897	1.173	Non-luminescent
X30-1-4	3836.605	21.434	975.685	2.051	98.019	5.859	Dark red
J10-1-1	916.249	26.795	652.403	6.703	107.107	7.337	Rose red
J10-1-2	570.723	21.05	375.556	4.015	103.043	3.818	Bright orange
J2-1-1	182.408	75.476	3361.26	5.076	121.08	2.669	Non-luminescent
J2-1-2	656.939	18.144	325.012	5.16	177.041	5.318	Dark red
X35-1-1	12.644	248.502	326.693	1.504	23.079	0.086	Weak dark red
X35-1-2	381.819	86.809	1590.628	4.324	71.326	1.172	Rose red
J13-1-1	2827.238	145.416	10237.084	41.164	149.967	17.231	Rose red
J13-1-2	3126.753	39.558	303.584	2.764	218.73	6.619	Rose red
J13-1-3	2131.043	79.872	278.163	2.599	180.257	4.225	Rose red
J13-1-4	1260.037	44.219	554.898	41.28	186.999	34.117	Rose red
J13-1-5	768.991	93.037	738.851	9.035	215.013	7.784	Non-luminescent
C07-1	654.762	104.159	2416.896	6.545	100.702	4.861	Rose red
C07-2	41.863	105.888	1243.504	7.159	81.73	1.593	Rose red
C07-3	424.762	100.53	1486.3	4.847	82.746	4.129	Dark red
C07-4	735.195	93.506	1203.761	4.293	80.711	4.327	Dark red
C07-5	1771.703	121.259	2040.433	9.723	105.213	9.369	Dark red
C07-6	1917.654	103.413	1194.318	5.932	98.126	14.894	Dark red
C12-1	68.894	67.801	759.24	3.174	104.248	0.617	Dark red
C12-2	69.928	85.663	588.988	11.606	74.268	0.801	Dark red
C12-3	73.557	97.144	646.253	2.717	58.909	0.959	Dark red
C12-4	79.126	68.77	1464.928	2.76	87.06	0.512	Dark red
C12-5	425.349	210.659	4258.032	28.923	60.088	3.54	Dark red
C12-6	105.184	76.754	1082.675	4.351	56.239	1.638	Dark red
C15-2	0.623	44.123	544.042	0.59	445.057	0.949	Dark red
C15-3	15.237	59.485	1691.713	7.326	206.355	0.463	Dark red
C15-4	231.302	67.323	646.773	18.216	153.648	2.295	Dark red
C15-5	1015.077	72.058	1271.933	9.552	120.783	3.696	Weak orange-red

Note: X represents “Xiweikou”; J represents “Jueshangu”; C represents “Caojiagou”. The same applies below.

Zn content ranges from 0.359 ppm to 28.923 ppm, with an average of 5.312 ppm. Ba content ranges from 0.166 ppm to 26.448 ppm, with an average of 4.059 ppm. Fe content ranges from 206.289 ppm to 26652.837 ppm, with an average of 6447.149 ppm. Mn content ranges from 2.205 ppm to 1352.904 ppm.

A line chart was plotted comparing the average values of each element for micritic to finely crystalline dolomites and sandy crystalline dolomites. It was found that the Na_2O, K_2O, Sr, Zn, and Ba content in micritic to finely crystalline dolomites is higher than in sandy crystalline dolomites. In contrast, sandy crystalline dolomites have higher Fe and Mn content. This indicates that the diagenetic intensity of sandy crystalline dolomites is greater than that of micritic to finely crystalline dolomites (Fig. 4).

3.2.5. Rare earth elements

Using LA-ICP-MS, 60 sets of rare earth element data were measured. Before data analysis, the experimental data were normalized using the average values of rare earth elements in post-

Table 3
Major element content in dolomites ($\omega(B)/10^{-2}$).

Sample ID	Na_2O	MgO	CaO	K_2O	Sample ID	Na_2O	MgO	CaO	K_2O	Sample ID	Na_2O	MgO	CaO	K_2O	Sample ID	Na_2O	MgO	CaO	K_2O
C07-1	0	21.34	30.565	0.056	J13-3	0.08	19.234	33.535	0.052	X14-1-4	0	21.622	30.089	0	X5-1-1	0.061	21.428	30.1	0.003
C07-10	0.033	21.433	30.016	0.005	J13-4	0.041	11.654	39.963	0.353	X14-1-5	0	22.282	30.125	0.011	X5-1-2	0.087	21.75	29.494	0.087
C07-11	0.035	21.425	29.985	0.048	J13-5	0.054	17.496	30.159	0.057	X14-1-7	0.036	22.148	30.267	0	X5-1-3	0.09	21.557	30.328	0.033
C07-12	0.027	19.846	31.092	0.018	J13-6	0.449	5.905	47.928	0.163	X14-1-9	0.02	22.058	30.025	0	X5-1-4	0.096	21.808	29.431	0.041
C07-13	0.02	20.507	31.385	0	J13-7	0.18	16.832	33.498	0.109	X15-1-2	0.156	12.721	32.826	0.044	X5-1-5	0.058	21.656	29.392	0.003
C07-2	0.007	21.575	30.126	0.025	J13-8	0.131	20.671	31.834	0.084	X15-1-3	0.022	21.855	30.157	0.025	X5-1-6	0.045	21.783	30.17	0.073
C07-3	0.042	21.85	30.212	0.009	J13-9	0.647	20.757	31.657	0.227	X15-1-4	0.049	21.483	30	0.101	X5-2-1	0.002	21.695	30.169	0.003
C07-4	0.047	21.849	30.609	0	J2-1-1	0.045	20.498	32.439	0.005	X15-1-5	0.057	19.404	29.034	0.048	X5-2-10	0.059	20.398	29.855	0
C07-5	0.035	21.588	30.681	0.023	J2-1-3	0.039	20.491	32.227	0.059	X30-1-1	0.167	0.169	54.794	0.137	X5-2-11	0.046	20.365	29.997	0.02
C07-6	0.084	21.277	29.931	0.052	J2-1-4	0.034	20.986	31.563	0	X30-1-2	0.126	0.235	54.956	0.063	X5-2-12	0.018	20.608	29.877	0
C07-7	0.009	21.098	29.71	0.039	J2-1-5	0.048	18.455	34.068	0.016	X30-1-3	0.007	3.662	51.275	0.039	X5-2-13	0.043	20.952	29.66	0
C07-8	0.108	22.135	30.611	0.046	J2-1-6	0.055	18.91	32.922	0.03	X30-1-4	0.011	21.592	29.96	0.136	X5-2-14	0.052	21.951	30.006	0.019
C07-9	0.062	21.559	30.499	0.025	J2-1-7	0.058	0.383	55.613	0	X30-1-5	0	0.349	55.618	0	X5-2-2	0.038	22.21	30.382	0
C12-1	0	21.365	30.673	0.026	J2-1-8	0.044	0.188	56.543	0.014	X30-1-6	0.031	20.942	29.785	0.075	X5-2-3	0.085	21.688	29.497	0.022
C12-10	0.038	20.847	30.735	0.034	X10-3-1	0.009	21.775	29.741	0.08	X30-1-7	0	0.551	54.205	0.088	X5-2-4	0.06	21.523	28.305	0
C12-11	0.049	21.413	31.094	0	X10-3-3	0.036	21.539	29.865	0.069	X30-1-8	0.014	0.422	53.745	0.126	X5-2-5	0.072	22.186	30.331	0.056
C12-2	0.134	22.289	29.94	0.048	X10-3-5	0.018	21.647	30.335	0.05	X30-1-9	0.041	1.552	54.372	0.038	X5-2-6	0.025	22.067	30.351	0.017
C12-3	0.007	21.734	30.373	0.016	X10-3-7	0.065	22.01	30.014	0.042	X35-1-1	0.027	0.174	56.703	0.014	X5-2-7	0.079	21.869	30.27	0.017
C12-4	0.083	20.683	32.348	0.014	X11-1-1	0.062	21.657	29.865	0.023	X35-1-10	0	0.242	56.387	0.007	X5-2-8	0.069	21.887	29.957	0.034
C12-5	0.074	21.356	29.819	0	X11-1-10	0.122	20.795	29.032	0.278	X35-1-11	0.022	22.174	30.247	0.012	X5-2-9	0.088	21.404	29.591	0.02
C12-6	0.081	21.97	30.378	0.022	X11-1-11	0.063	20.452	29.278	0.032	X35-1-2	0	22.411	30.186	0.002	X6-4-1	0.009	21.933	29.506	0.017
C12-9	0.216	21.217	31.14	0.031	X11-1-12	0.037	17.762	29.28	0	X35-1-3	0.226	22.032	30.287	0.073	X6-4-10	0	21.563	30.201	0.022
C15-1	0.027	21.309	30.862	0.022	X11-1-13	0.034	20.4	29.566	0.005	X35-1-4	0.097	0.441	55.976	0.037	X6-4-11	0.089	21.918	29.539	0.026
C15-2	0.069	20.996	31.385	0.031	X11-1-14	0.025	19.883	29.439	0.014	X35-1-5	0.031	0.172	56.275	0.001	X6-4-12	0.035	21.712	29.777	0.068
C15-4	0.022	0.521	55.051	0	X11-1-15	0.024	21.517	30.069	0.043	X35-1-6	0.099	0.189	58.181	0.04	X6-4-13	0.2	20.67	30.699	0.1
J10-1-10	0.077	21.102	31.16	0.02	X11-1-16	0.04	21.872	30.446	0.038	X35-1-7	0.13	22.461	30.618	0.05	X6-4-14	0.064	22.543	29.429	0.003
J10-1-3	0.027	20.913	31.474	0.011	X11-1-17	0.029	21.936	30.346	0	X35-1-8	0.039	0.165	55.595	0	X6-4-15	0	21.836	29.4	0.002
J10-1-4	0	0.76	54.382	0	X11-1-18	0.015	21.945	30.49	0.005	X35-1-9	0.016	21.605	30.479	0.002	X6-4-16	0.016	21.771	30.378	0.026
J10-1-5	0.005	20.358	32.095	0.008	X11-1-19	0.086	21.646	29.556	0.13	X4-3-1	0.044	0.632	55.666	0.02	X6-4-17	0.018	21.118	29.746	0.054
J10-1-8	0.036	20.592	31.495	0.041	X11-1-3	0.051	21.403	29.787	0.156	X4-3-10	0.138	22.334	30.016	0.025	X6-4-18	0.04	21.371	29.647	0.002
J10-1-9	0.022	0.275	55.412	0.019	X11-1-5	0.184	21.756	29.958	0.092	X4-3-11	0.052	22.497	29.548	0.032	X6-4-19	0.063	19.729	29.277	0.034
J13-1	0.081	19.59	33.664	0.052	X11-1-6	0.117	21.728	29.834	0.113	X4-3-13	0.034	22.1	30.085	0.003	X6-4-2	0.007	19.962	30.017	0.009
J13-11	0.005	0.597	57.399	0.006	X11-1-8	0.022	21.957	30.152	0.057	X4-3-2	0.086	21.915	30.039	0.036	X6-4-20	0.153	19.319	29.309	0.037
J13-12	0.009	17.751	33.595	0.043	X11-1-9	0.093	21.603	29.603	0.136	X4-3-3	0.12	21.77	29.911	0.049	X6-4-21	0.096	18.842	29.226	0
J13-13	0.027	19.05	32.166	0.143	X14-1-1	0.104	19.394	28.947	0.062	X4-3-4	0.017	0.117	56.277	0.022	X6-4-3	0	18.559	31.743	0
J13-14	0.038	19.207	32.789	0.051	X14-1-10	0.043	21.966	30.416	0.025	X4-3-5	0.037	0.246	56.586	0.016	X6-4-4	0.055	22.044	30.014	0.009
J13-17	0.012	1.015	54.4	0.072	X14-1-11	0	21.569	29.991	0.017	X4-3-6	0.039	0.378	55.431	0.02	X6-4-5	0.031	21.35	29.722	0.041
J13-18	0.022	20.524	32.823	0	X14-1-12	0.027	21.713	29.139	0.006	X4-3-7	0.061	22.077	30.061	0.02	X6-4-6	0.029	20.776	31.726	0
J13-19	0.013	18.307	32.792	0.009	X14-1-2	0.029	22.393	29.877	0.014	X4-3-8	0.079	21.242	29.719	0.147	X6-4-7	0.02	18.791	32.295	0
J13-2	0.309	17.664	33.385	0.102	X14-1-3	0.002	22.27	30.554	0.026	X4-3-9	0.075	22.26	29.409	0.038	X6-4-8	0.018	21.463	29.548	0.043
															X6-4-9	0.009	21.686	29.136	0.005

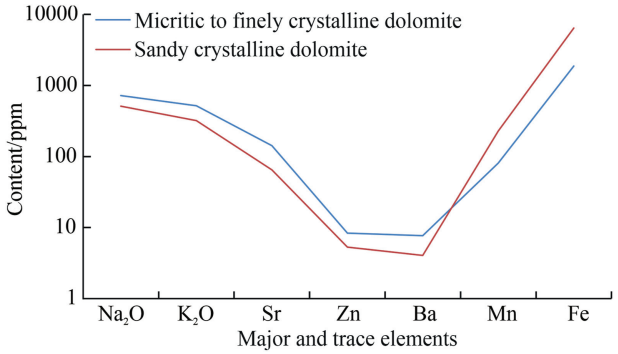

Fig. 4. Line chart of average major and trace elements in dolomites of different grain sizes.

Archean Australian shale (PAAS). The analysis focused on ΣREE, LREE and HREE, REE distribution patterns, and δEu and δCe characteristics of micritic to finely crystalline dolomites and sandy crystalline dolomites (Tables 4 and 5).

A total of 21 points were tested for micritic to finely crystalline dolomites, with ΣREE ranging from 6.172 ppm to 113.604 ppm, and an average of 33.67 ppm. For sandy crystalline dolomites, 39 points were tested, with ΣREE ranging from 3.62 ppm to 159.485 ppm, and an average of 24.619 ppm. Overall, the total rare earth element content in micritic to finely crystalline dolomites is higher than that in sandy crystalline dolomites, which is related to the migration and depletion of rare earth elements during dolomitization.

The ΣLREE of micritic to finely crystalline dolomites ranges from 5.498 ppm to 78.918 ppm, with an average of 29.053 ppm. The ΣHREE ranges from 0.674 ppm to 34.685 ppm, with an average of 5.617 ppm. The ΣLREE/ΣHREE ratio ranges from 0.887 to 13.356, with an average of 6.968. For sandy crystalline dolomites, the ΣLREE ranges from 2.967 ppm to 153.61 ppm, with an average of 22.505 ppm. The ΣHREE ranges from 0.386 ppm to 10.954 ppm, with an average of 2.114 ppm. The ΣLREE/ΣHREE ratio ranges from 2.792 to 26.148, with an average of 6.968. Overall, micritic to finely crystalline dolomites are relatively enriched in both light and heavy rare earth elements, while sandy crystalline dolomites lose light rare earth elements through recrystallization during the later burial stage, resulting in a greater depletion of heavy rare earth elements.

The distribution patterns of rare earth elements can be studied by plotting line graphs of various rare earth elements for each test point. From the REE distribution patterns of micritic to finely crystalline dolomites and sandy crystalline dolomites, it can be observed that all sample test points show relatively high values for Eu and Gd, forming a convex shape in the line graphs at these two elements. Light rare earth elements in micritic to finely crystalline dolomites show a leftward inclination, while heavy rare earth elements, except for some test points in the Jueshangu section, show a rightward inclination overall. Sandy crystalline dolomites exhibit a clear leftward inclination for light rare earth elements and a clear rightward inclination for heavy rare earth elements. This indicates the migration and depletion of rare earth elements during diagenesis, with a greater degree of depletion for heavy rare earth elements [5,26,41] (Fig. 5).

The δCe values of the test points range from 0.291 to 1.319, with an average of 0.993, while δEu ranges from 0.459 to 1.268, with an average of 0.847. Overall, there is no significant Ce anomaly, but the δEu values are relatively low, indicating a weak Eu depletion. From the relationship graph of δCe and δEu, it can be observed that the Ce negative anomaly is not very pronounced in micritic to finely crystalline dolomites, while the Eu negative anomaly is evident, indicating a low-temperature alkaline environment. Some micritic to finely crystalline dolomites show significant negative anomalies for both Ce and Eu, suggesting that these dolomites generally formed in a low-temperature, alkaline, weakly oxidizing environment. In the δCe and δEu relationship graph for sandy crystalline dolomites, some test points show positive Eu anomalies and negative Ce anomalies, indicating that the formation of these dolomites is more related to high-temperature oxidizing environments during later compaction and burial [25,27,41] (Fig. 6).

3.2.6. Cathodoluminescence

Micritic to finely crystalline dolomites emit rose-red to dark red light under cathodoluminescence (Fig. 7(b–d), (f)). For instance, sample XWK35-1 from the upper Majiagou Formation is a fine crystalline dolomite emitting rose-red light. The fine crystalline dolomite has Fe content of 1590.628 ppm, Mn content of 86.809 ppm, Fe/Mn ratio of 18.323, and Sr content of 71.326 ppm (Table 2, X35-1-2). Cathodoluminescence reveals banded calcite clusters filling fractures, with calcite having Fe content of 326.693 ppm, Mn content of 248.502 ppm, and Sr content of 23.079 ppm (Table 2, X35-1-1). Generally, bright calcite emits dim light, with the formation of bright bands related to progressive burial and pore water evolution, showing a non-luminescent to bright to dim luminescence pattern. Sample X30-1 shows micritic dolomite as brownish-yellow nodules emitting dark red light, with Fe content of 1740.222 ppm, Mn content of 58.632 ppm, Fe/Mn ratio of 29.680, and Sr content of 95.379 ppm (Table 2, X30-1-1). The surrounding rock calcite emits weak dark orange-red light, with Fe content of 1061.425 ppm, Mn content of 22.281 ppm, Fe/Mn ratio of 47.640, and Sr content of 87.837 ppm (Table 2, X30-1-2). Additionally, bright calcite filling fractures emits weak orange-red light, with Fe content of 341.316 ppm, Mn content of 12.835 ppm, and Sr content of 141.897 ppm (Table 2, X30-1-3) (Fig. 7(d)). In the late diagenetic stage, Fe^{2+}-bearing pore water can migrate along fractures under compaction, forming ferroan calcite when interacting with calcite, resulting in weaker cathodoluminescence of calcite cement Carroll, 1958. Sample JSG13-1 is a coarse crystalline dolomite showing zonal structures in dolomite crystals under cathodoluminescence, with sequential bright-dim-bright luminescence from the core to the periphery. Fe and Mn content tests were performed at two positions in the dolomite (Table 2, J13-1-2, J13-1-3, J13-1-4, and J13-1-5), revealing that the Fe/Mn ratio in the dim parts is lower than that in the bright peripheral parts (Fig. 7f). The cathodoluminescence properties of micritic to finely crystalline dolomites are more significantly influenced by Fe content than Mn content, with luminescence increasing as Fe content decreases.

For sandy crystalline dolomites (fine, medium, and coarse crystalline), cathodoluminescence intensity decreases as dolomite crystal size increases, with thin sections mainly showing dark red to non-luminescent light, see Fig. 7(h)–(j), (l), (n), (p). This type of dolomite typically forms in closed systems, not following the general rule of increasing Fe and Mn content with increasing diagenetic intensity in open systems. These dolomites generally form in burial environments [3].

The cathodoluminescence (CL) characteristics of dolomite exhibit significant changes across different diagenetic stages, reflecting the diversity of diagenetic environments. During the marine sedimentation stage, the low concentrations of Fe and Mn in seawater lead to similarly low levels of Fe and Mn in the original marine carbonate minerals, resulting in the mudstone and cement typically exhibiting no luminescence under cathodoluminescence. In the paragenetic dolomitization process, the fine-grained and microcrystalline dolomites begin to enrich in Mn^{2+} and Fe^{3+}, with CL characteristics displaying weak to moderate red luminescence and generally flat distribution curves, indicating the evolution of dolomite composition and diagenetic processes. In the meteoric

Table 4
REE content in dolomite samples (ppm).

Sample ID	La	Ce	Pr	Nd	Sm	Eu	Gd	Tb	Dy	Ho	Er	Tm	Yb	Lu	ΣREE	ΣLREE	ΣHREE	ΣLREE/ΣHREE	δCe	δEu
X5-1-1	1.797	3.892	0.392	1.468	0.281	0.063	0.612	0.043	0.25	0.05	0.141	0.017	0.116	0.017	9.139	7.892	1.247	6.33	1.07	0.644
X5-1-2	1.516	3.36	0.315	1.204	0.23	0.042	0.316	0.031	0.183	0.041	0.111	0.014	0.09	0.012	7.465	6.667	0.798	8.357	1.12	0.711
X5-2-1	0.118	1.062	0.234	1.136	0.359	0.056	0.227	0.041	0.198	0.032	0.075	0.009	0.061	0.009	3.62	2.967	0.653	4.543	0.902	0.92
X5-2-2	0.824	8.347	1.801	8.943	1.986	0.418	1.175	0.209	1.121	0.195	0.472	0.058	0.384	0.053	25.986	22.318	3.668	6.085	0.93	1.268
X5-2-3	0.863	4.244	0.656	2.647	0.569	0.089	0.404	0.058	0.31	0.058	0.138	0.018	0.114	0.018	10.187	9.069	1.118	8.11	1.101	0.874
X5-2-4	0.595	2.55	0.435	2.115	0.641	0.137	0.484	0.081	0.425	0.077	0.195	0.023	0.152	0.02	7.928	6.472	1.456	4.444	0.989	1.158
X5-2-5	1.371	2.882	0.29	1.051	0.198	0.039	0.284	0.03	0.175	0.035	0.089	0.011	0.066	0.012	6.533	5.831	0.702	8.305	1.054	0.742
X5-2-6	2.342	5.477	0.59	2.14	0.431	0.086	0.603	0.054	0.361	0.076	0.206	0.028	0.175	0.027	12.596	11.066	1.529	7.235	1.074	0.769
X5-2-7	2.169	5.051	0.537	1.932	0.407	0.088	0.51	0.066	0.425	0.087	0.24	0.031	0.198	0.032	11.772	10.185	1.587	6.416	1.079	0.894
X4-3-1	1.346	2.909	0.309	1.227	0.247	0.06	0.623	0.034	0.202	0.041	0.111	0.015	0.095	0.013	7.234	6.099	1.135	5.373	1.04	0.623
X4-3-2	1.231	2.583	0.272	1.054	0.196	0.039	0.423	0.029	0.176	0.038	0.107	0.014	0.076	0.013	6.251	5.375	0.876	6.137	1.031	0.574
X4-3-3	0.432	0.577	0.321	1.562	0.344	0.064	0.295	0.05	0.316	0.068	0.195	0.03	0.199	0.03	4.481	3.299	1.182	2.792	0.304	0.941
X4-3-4	1.185	2.6	0.275	1.05	0.203	0.042	0.254	0.024	0.167	0.035	0.094	0.013	0.076	0.011	6.029	5.355	0.674	7.947	1.051	0.859
X6-4-1	2.2	5.063	0.584	2.099	0.437	0.102	0.466	0.061	0.363	0.065	0.186	0.025	0.146	0.024	11.82	10.484	1.335	7.852	1.029	1.054
X6-4-2	2.171	5.077	0.599	2.123	0.454	0.098	0.418	0.056	0.35	0.065	0.182	0.024	0.161	0.024	11.803	10.522	1.281	8.217	1.023	1.063
X6-4-3	16.194	75.249	11.953	43.445	6.081	0.688	3.333	0.311	1.304	0.191	0.399	0.043	0.257	0.036	159.485	153.61	5.875	26.148	1.064	0.703
X6-4-4	10.296	53.447	10.898	50.046	9.587	1.667	5.434	0.695	3.006	0.432	0.822	0.082	0.425	0.057	146.893	135.939	10.954	12.41	0.893	1.067
X6-4-5	8.572	50.783	9.558	41.216	7.764	1.341	4.367	0.617	2.683	0.397	0.811	0.088	0.463	0.057	128.718	119.235	9.482	12.575	0.976	1.063
X6-4-6	8.281	41.464	7.95	34.569	5.823	0.975	3.356	0.445	2.09	0.34	0.761	0.084	0.48	0.064	106.683	99.062	7.62	13	0.933	1.02
X6-4-7	7.905	39.219	7.427	31.885	5.314	0.88	3.132	0.41	1.963	0.336	0.771	0.087	0.51	0.072	99.909	92.629	7.28	12.723	0.94	1
X10-3-1	2.538	5.745	0.711	2.705	0.58	0.136	0.919	0.081	0.506	0.093	0.259	0.036	0.232	0.033	14.574	12.415	2.159	5.749	0.982	0.833
X10-3-2	1.998	4.502	0.554	2.145	0.516	0.112	0.691	0.076	0.488	0.092	0.241	0.031	0.179	0.027	11.653	9.827	1.826	5.383	0.983	0.857
X11-1-1	2.574	5.553	0.664	2.575	0.558	0.12	0.97	0.075	0.464	0.094	0.261	0.036	0.226	0.034	14.203	12.043	2.16	5.575	0.979	0.723
X11-1-2	2.382	4.983	0.572	2.121	0.41	0.084	0.502	0.065	0.385	0.075	0.213	0.029	0.179	0.026	12.025	10.552	1.474	7.16	0.985	0.856
X11-1-3	2.339	5.622	0.686	2.41	0.528	0.114	0.554	0.077	0.479	0.092	0.255	0.034	0.213	0.032	13.435	11.699	1.736	6.739	1.016	0.985
X14-1-1	1.702	3.856	0.415	1.536	0.323	0.06	0.422	0.044	0.291	0.06	0.173	0.024	0.149	0.024	9.08	7.893	1.187	6.649	1.058	0.753
X14-1-2	1.673	3.792	0.399	1.499	0.323	0.081	0.898	0.049	0.325	0.065	0.183	0.025	0.176	0.025	9.513	7.766	1.746	4.448	1.07	0.6
X14-1-3	1.42	3.37	0.376	1.393	0.276	0.065	0.341	0.053	0.342	0.064	0.178	0.027	0.173	0.025	8.103	6.9	1.203	5.738	1.062	0.976
X14-1-4	1.863	4.084	0.428	1.443	0.296	0.052	0.347	0.044	0.255	0.056	0.158	0.022	0.159	0.022	9.228	8.166	1.062	7.686	1.055	0.757
X15-1-1	12.209	34.64	3.619	13.863	3.382	0.696	3.251	0.454	2.882	0.558	1.542	0.208	1.383	0.2	78.888	68.409	10.479	6.528	1.193	0.986
X30-1-1	1.889	5.445	0.717	3.097	0.769	0.145	0.656	0.088	0.5	0.095	0.251	0.036	0.223	0.033	13.944	12.062	1.882	6.407	1.047	0.963
X30-1-2	2.602	6.039	0.689	2.546	0.504	0.096	0.666	0.07	0.43	0.091	0.248	0.034	0.231	0.032	14.278	12.476	1.803	6.921	1.038	0.76
X30-1-3	1.235	3.036	0.353	1.351	0.253	0.045	0.245	0.034	0.218	0.042	0.121	0.017	0.117	0.017	7.084	6.273	0.812	7.728	1.055	0.854
X30-1-4	3.111	9.248	1.088	4.192	0.861	0.151	0.753	0.086	0.526	0.103	0.286	0.04	0.258	0.039	20.742	18.651	2.091	8.92	1.135	0.881
J10-1-1	3.095	9.068	1.199	4.568	0.896	0.182	0.844	0.103	0.6	0.122	0.347	0.051	0.32	0.051	21.445	19.007	2.438	7.798	1.051	0.985
J10-1-2	2.475	6.745	0.85	3.158	0.587	0.116	0.574	0.076	0.405	0.083	0.233	0.032	0.216	0.035	15.584	13.93	1.654	8.423	1.052	0.942
J2-1-1	7.155	17.909	2.336	8.713	1.442	0.218	1.319	0.177	1.101	0.213	0.568	0.074	0.472	0.066	41.764	37.774	3.99	9.467	0.996	0.743
J2-1-2	1.742	3.226	0.339	1.171	0.198	0.038	0.342	0.025	0.146	0.031	0.081	0.011	0.078	0.012	7.44	6.713	0.727	9.237	0.965	0.652
X35-1-1	0.993	0.866	0.432	2.396	0.885	0.244	1.316	0.277	1.968	0.472	1.346	0.164	0.881	0.136	12.375	5.816	6.559	0.887	0.291	1.024
X35-1-2	9.539	21.066	2.428	9.187	1.634	0.357	1.483	0.171	0.825	0.148	0.359	0.043	0.246	0.035	47.521	44.211	3.31	13.356	1.009	1.078
J13-1-1	16.187	34.52	4.218	18.05	5.334	0.61	6.991	1.17	8.787	2.022	6.621	1.023	6.991	1.081	113.604	78.918	34.685	2.275	0.962	0.459
J13-1-2	16.143	30.625	3.023	10.886	2.074	0.464	2.989	0.349	2.317	0.517	1.567	0.217	1.463	0.238	72.871	63.214	9.657	6.546	1.006	0.846
J13-1-3	12.936	26.737	2.756	10.153	2.004	0.452	2.541	0.326	2.319	0.527	1.626	0.238	1.59	0.256	64.462	55.039	9.424	5.84	1.032	0.924
J13-1-4	15.816	30.393	3.053	11.346	2.226	0.511	3.464	0.381	2.705	0.599	1.848	0.272	1.85	0.295	74.76	63.346	11.414	5.55	1.005	0.827
J13-1-5	15.109	31.453	3.392	12.703	2.686	0.624	3.199	0.402	2.751	0.602	1.85	0.266	1.785	0.289	77.111	65.967	11.145	5.919	1.014	0.987
C07-1	2.545	5.166	0.571	2.157	0.43	0.087	0.567	0.058	0.342	0.072	0.193	0.026	0.157	0.025	12.396	10.955	1.44	7.606	0.989	0.807
C07-2	1.939	3.493	0.381	1.35	0.241	0.051	0.379	0.033	0.201	0.04	0.105	0.014	0.08	0.012	8.32	7.456	0.864	8.625	0.935	0.763
C07-3	1.609	3.002	0.328	1.078	0.189	0.035	0.331	0.031	0.156	0.031	0.084	0.011	0.067	0.01	6.961	6.241	0.72	8.665	0.952	0.624
C07-4	1.381	2.446	0.252	0.915	0.153	0.035	0.286	0.024	0.132	0.026	0.072	0.009	0.051	0.008	5.789	5.181	0.607	8.533	0.949	0.722
C07-5	3.163	6.186	0.662	2.39	0.473	0.086	0.653	0.052	0.325	0.064	0.177	0.023	0.149	0.021	14.425	12.961	1.464	8.852	0.985	0.709

(*continued on next page*)

Table 4 (*continued*)

Sample ID	La	Ce	Pr	Nd	Sm	Eu	Gd	Tb	Dy	Ho	Er	Tm	Yb	Lu	ΣREE	ΣLREE	ΣHREE	ΣLREE/ΣHREE	δCe	δEu
C07-6	2.158	4.285	0.456	1.649	0.314	0.069	0.585	0.044	0.267	0.053	0.147	0.02	0.125	0.018	10.19	8.932	1.259	7.096	0.995	0.704
C12-1	1.102	2.052	0.193	0.713	0.109	0.022	0.204	0.013	0.085	0.018	0.046	0.006	0.037	0.005	4.605	4.19	0.415	10.107	1.017	0.636
C12-2	1.053	1.71	0.166	0.558	0.098	0.021	0.172	0.013	0.09	0.018	0.048	0.006	0.035	0.005	3.993	3.606	0.386	9.332	0.927	0.714
C12-3	1.316	1.995	0.183	0.658	0.102	0.023	0.199	0.016	0.1	0.021	0.059	0.007	0.045	0.006	4.73	4.278	0.453	9.446	0.908	0.695
C12-4	1.075	1.959	0.196	0.676	0.13	0.026	0.169	0.017	0.116	0.023	0.061	0.008	0.045	0.007	4.507	4.061	0.445	9.117	0.979	0.795
C12-5	1.772	4.887	0.412	1.661	0.308	0.073	0.377	0.04	0.239	0.052	0.123	0.016	0.106	0.014	10.08	9.113	0.968	9.418	1.319	0.986
C12-6	0.944	1.933	0.198	0.676	0.142	0.03	0.194	0.018	0.11	0.025	0.067	0.008	0.054	0.008	4.408	3.924	0.484	8.107	1.029	0.815
C15-3	1.498	4.292	0.607	2.558	0.573	0.106	0.531	0.082	0.528	0.097	0.268	0.033	0.221	0.036	11.429	9.633	1.796	5.365	0.999	0.903
C15-4	1.971	3.948	0.457	1.773	0.393	0.077	0.436	0.054	0.358	0.077	0.214	0.028	0.173	0.024	9.985	8.62	1.366	6.312	0.959	0.863
C15-5	1.3	2.62	0.291	1.041	0.201	0.044	0.269	0.024	0.155	0.034	0.086	0.013	0.081	0.013	6.172	5.498	0.674	8.157	0.982	0.871

diagenesis stage (late Caledonian to Hercynian), rocks undergo atmospheric freshwater leaching and ancient karst processes; near-surface oxidizing conditions lead to low levels of Fe^{2+} and Mn^{2+} in pore water, causing the granular bright calcite cements to exhibit non-luminescence or dull luminescence. During the burial diagenesis stage, dolomites are typically coarse to very coarse crystalline, often exhibiting cloudy cores and boundary structures, with CL characteristics ranging from weak to strong red luminescence. Dolomite cements frequently show banded structures that luminesce under cathodoluminescence; when Fe content exceeds 10,000 ppm, non-luminescence may occur. The rare earth element distribution curves exhibit a distinct "cap-like" structure, indicating that LREEs are adsorbed by Mn hydroxides and HREEs by Fe hydroxides in weakly oxidizing pore waters, leading to the enrichment of MREEs. By comparing the CL characteristics of dolomites under different diagenetic conditions, we reveal the close relationship between these characteristics and geochemical data, enhancing our understanding of dolomite diagenesis and highlighting the importance of CL features as indicators of diagenetic processes.

3.2.7. Characteristics of fluid inclusions

Dolomitization processes in carbonate rocks can be distinguished by the temperature and salinity of the fluid inclusions, which vary depending on the diagenetic stage. Early diagenetic dolomitization typically occurs at temperatures below 50 °C with low salinities (0~10 wt% NaCl), indicating shallow burial and minimal deep fluid influence. In contrast, deep burial dolomitization occurs at higher temperatures (80 °C to over 150 °C) and salinities (15~24 wt% NaCl or higher), reflecting deeper burial depths and the influence of deep-seated, saline fluids [50–53]. Although fluid inclusion homogenization temperatures and salinities have not been directly measured in the study area, previous research by Su and Jiu indicates that temperatures typically exceed 50 °C, suggesting that the dolomites in this region have likely undergone deep burial diagenesis [3,54].

4. Discussion

4.1. Zonal cathodoluminescence and element characteristics of sandy crystalline dolomite

Dolomite located at the edges of intercrystalline pores or dissolution-enlarged pores generally develops well-defined zonal structures. These structures exhibit alternating pale gray-brown or dark red and bright orange-red luminescence from the interior to the exterior of the dolomite crystals, presenting luminescence features such as deep red - dark red - bright red or deep red - bright red - dark red. For example, the XWK5-2 rock sample, a medium to coarse crystalline dolomite, emits dark red light under cathodoluminescence. The zoned dolomite in the dissolution pores exhibits alternating dark red - weak dark red - non-luminescent - bright red luminescence from the center to the crystal edge. Analysis of the major and trace elements at different positions within the dolomite shows that the Fe and Mn contents initially increase and then decrease from the center to the edge of the dolomite crystals. Additionally, the Fe/Mn ratio is higher in the dark luminescent bands of the dolomite crystals, while the Na_2O and K_2O contents exhibit opposite trends to those of Fe and Mn (Figs. 6–2i, 8).

For dolomites with "cloudy core-bright rim" structures, the luminescence characteristics under cathodoluminescence are similar to those of zoned dolomite, but the entire dolomite may exhibit relatively uniform luminescence with no significant variation. For instance, the C07 rock sample, a coarse to very coarse

Table 5
Statistical content of different REE parameters in dolomites.

Parameter	Lithology	Minimum value	Maximum value	Average value
ΣREE	Micritic to finely crystalline dolomite	6.172 ppm	113.604 ppm	33.67 ppm
	Sandy crystalline dolomite	3.62 ppm	159.485 ppm	24.619 ppm
ΣLREE	Micritic to finely crystalline dolomite	5.498 ppm	78.918 ppm	29.053 ppm
	Sandy crystalline dolomite	2.967 ppm	153.61 ppm	22.505 ppm
ΣHREE	Micritic to finely crystalline dolomite	0.674 ppm	34.685 ppm	5.617 ppm
	Sandy crystalline dolomite	0.386 ppm	10.954 ppm	2.114 ppm
ΣLREE/ΣHREE	Micritic to finely crystalline dolomite	0.887	13.356	6.968
	Sandy crystalline dolomite	2.792	26.148	8.214
δCe	Micritic to finely crystalline dolomite	0.291	1.193	0.999
	Sandy crystalline dolomite	0.304	1.319	0.993
δEu	Micritic to finely crystalline dolomite	0.459	1.078	0.853
	Sandy crystalline dolomite	0.574	1.268	0.844

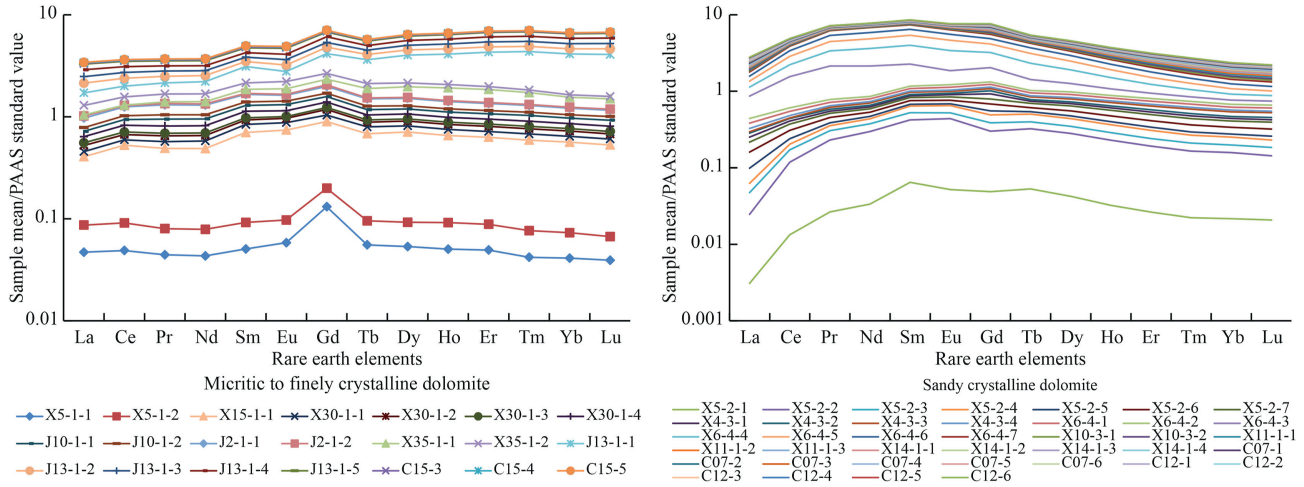

Fig. 5. Ree distribution patterns of dolomites.

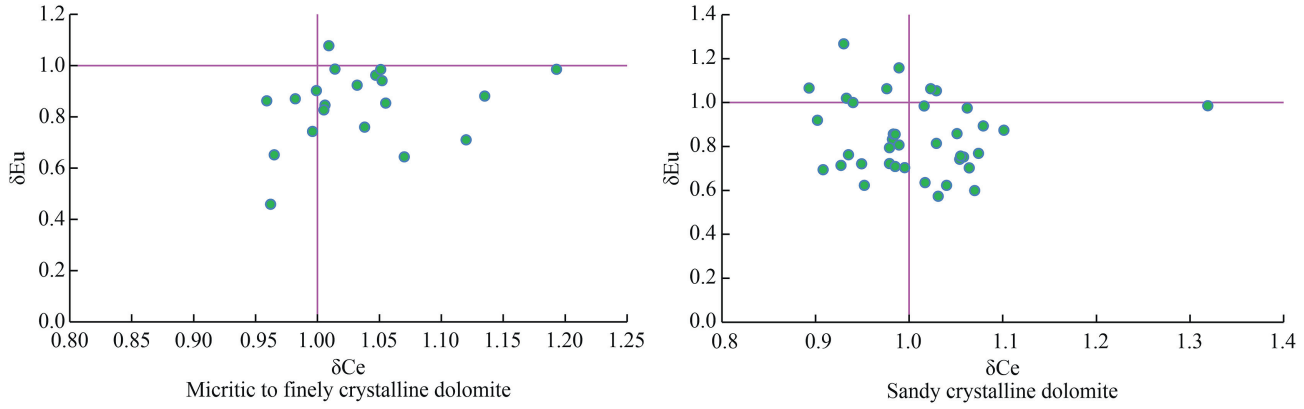

Fig. 6. Relationship between δCe and δEu in dolomites.

crystalline dolomite, shows a clear "cloudy core-bright rim" structure under the microscope. However, under cathodoluminescence, the dolomite crystal as a whole emits dark red light. The measured major and trace elements indicate relatively stable Fe and Mn contents, with Fe/Mn values ranging from 11.743 to 23.204. The Na content shows noticeable variation, with extremely low Na_2O values at the G07-7 position and extremely high values at the GJG07-8 position, while the K_2O content remains relatively stable (Figs. 7n and 9).

The differences in zonal and main crystal cathodoluminescence intensity and color in sandy crystalline dolomites suggest that the fluids forming the dolomite zones differ from the main crystal fluids and indicate multiple phases of fluid interaction. The bright red dolomite zones may have formed through over-dolomitization in a meteoric freshwater environment [3].

4.2. Genesis of dolomite

In recent years, many domestic scholars have studied the genesis of Ordovician dolomites in the Lower Paleozoic of the Ordos Basin (mainly in the Ma 5 submember of the central and eastern regions), deeply analyzing the genesis mechanism of dolomites and

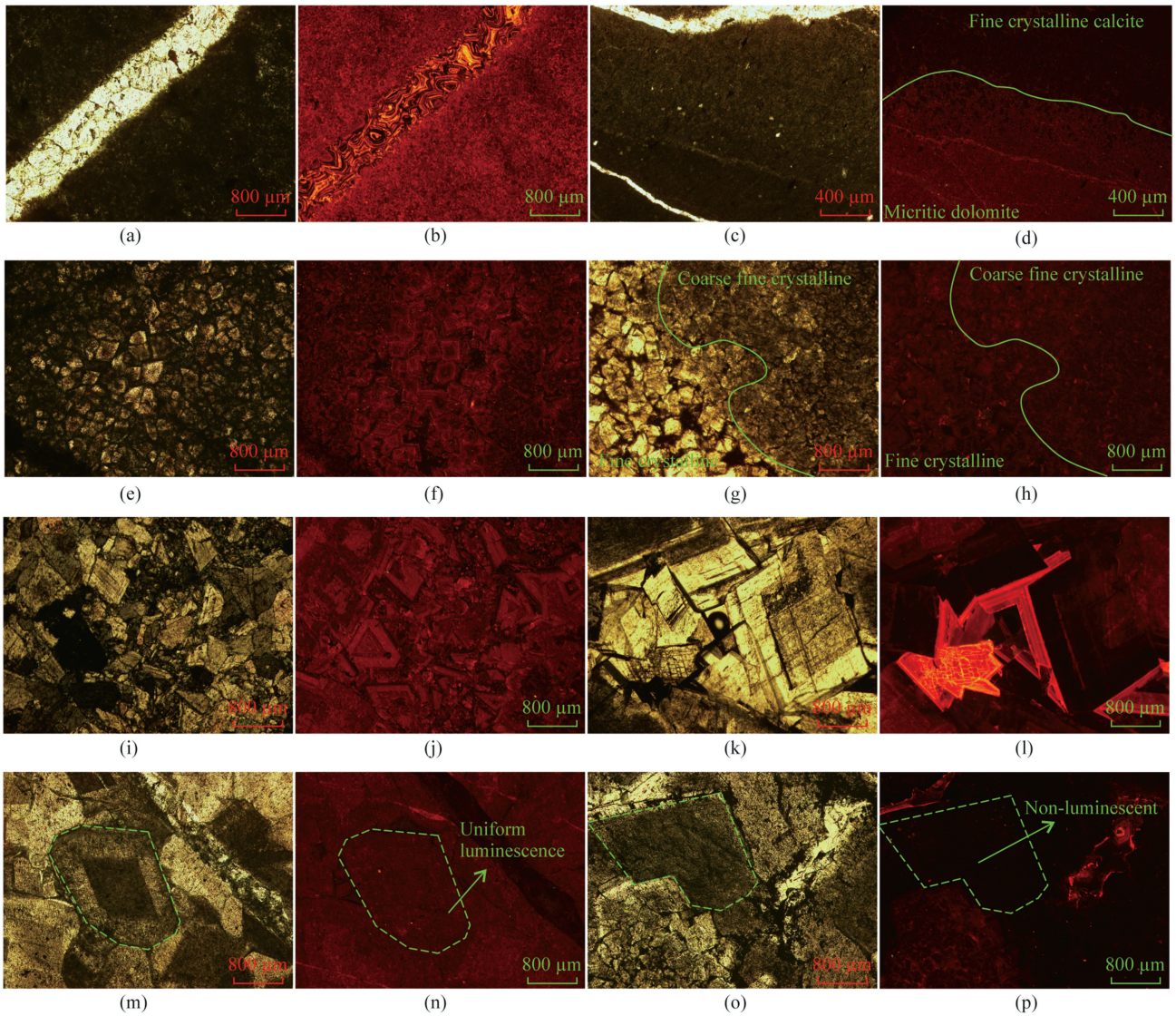

Fig. 7. Cathodoluminescence characteristics of dolomites. (a) calcareous fine crystalline dolomite, fractures filled with calcite, Xiweikou, Majiagou Formation, plane-polarized light (−); (b) calcareous fine crystalline dolomite, fine crystalline dolomite emits rose-red light, fracture calcite shows bright bands, Xiweikou, Majiagou Formation, cathodoluminescence; (c) micritic dolomite, fractures filled with calcite, Xiweikou, Majiagou Formation, plane-polarized light (−); (d) micritic dolomite, dolomite emits dark red light, calcite emits weak dark orange-red light, Xiweikou, Majiagou Formation, cathodoluminescence; (e) coarse crystalline dolomite, cloudy core-bright rim structure, Jueshangu, Ma 6 member, plane-polarized light (−); (f) coarse crystalline dolomite, emits dark red light, Jueshangu, Ma 6 member, cathodoluminescence; (g) fine crystalline dolomite, Xiweikou, Majiagou Formation, plane-polarized light (−); (h) fine crystalline dolomite, fine crystalline dolomite and coarse crystalline dolomite emit consistent dark red light, fracture calcite shows bright bands, Xiweikou, Majiagou Formation, cathodoluminescence; (i) medium crystalline dolomite, Caojiagou, Yeli-Liangjiashan Formation, plane-polarized light (+); (j) medium crystalline dolomite, shows alternating rose-red and dark red banded luminescence, Caojiagou, Yeli-Liangjiashan Formation, cathodoluminescence; (k) medium to coarse crystalline dolomite, dolomite has banded structure, Xiweikou, Majiagou Formation, plane-polarized light (−); (l) medium to coarse crystalline dolomite, coarse crystalline dolomite shows alternating dark red, weak dark red, non-luminescent, and bright red banded luminescence, Xiweikou, Majiagou Formation, cathodoluminescence; (m) coarse to very coarse crystalline dolomite, cloudy core-bright rim structure, Caojiagou, Yeli-Liangjiashan Formation, plane-polarized light (−); (n) coarse to very coarse crystalline dolomite, dolomite emits uniform dark red light, Caojiagou, Yeli-Liangjiashan Formation, cathodoluminescence; (o) fine crystalline dolomite, coarse crystalline dolomite filling dissolution pores, Xiweikou, Majiagou Formation, plane-polarized light (−); (p) fine crystalline dolomite, coarse crystalline dolomite non-luminescent, Xiweikou, Majiagou Formation, cathodoluminescence.

describing different dolomitization [5,15,23,25,26,30,31,38,55,56]. Summarizing these studies, it can be concluded that the formation of dolomites in most areas of the Ordovician in the Ordos Basin is related to three models: syn-sedimentary to penecontemporaneous dolomitization, penecontemporaneous to reflux dolomitization, and burial dolomitization. In some areas, microbial dolomitization and hydrothermal dolomitization also occur.

Micritic dolomites generally form in syn-sedimentary to penecontemporaneous evaporative environments. These dolomites typically form in low-energy, reducing depositional settings, have dark colors, moderate to low dolomite ordering, low Mg/Ca ratios, high Na and K contents, and low Mn and Fe contents. Finely crystalline dolomites are often formed by reflux dolomitization, where previously formed micritic dolomites, partially or completely detached from the depositional water body, enter a penecontemporaneous environment. High-salinity brines, under gravity, slowly percolate downward, causing further dolomitization of the micritic dolomites and forming euhedral dolomite. These

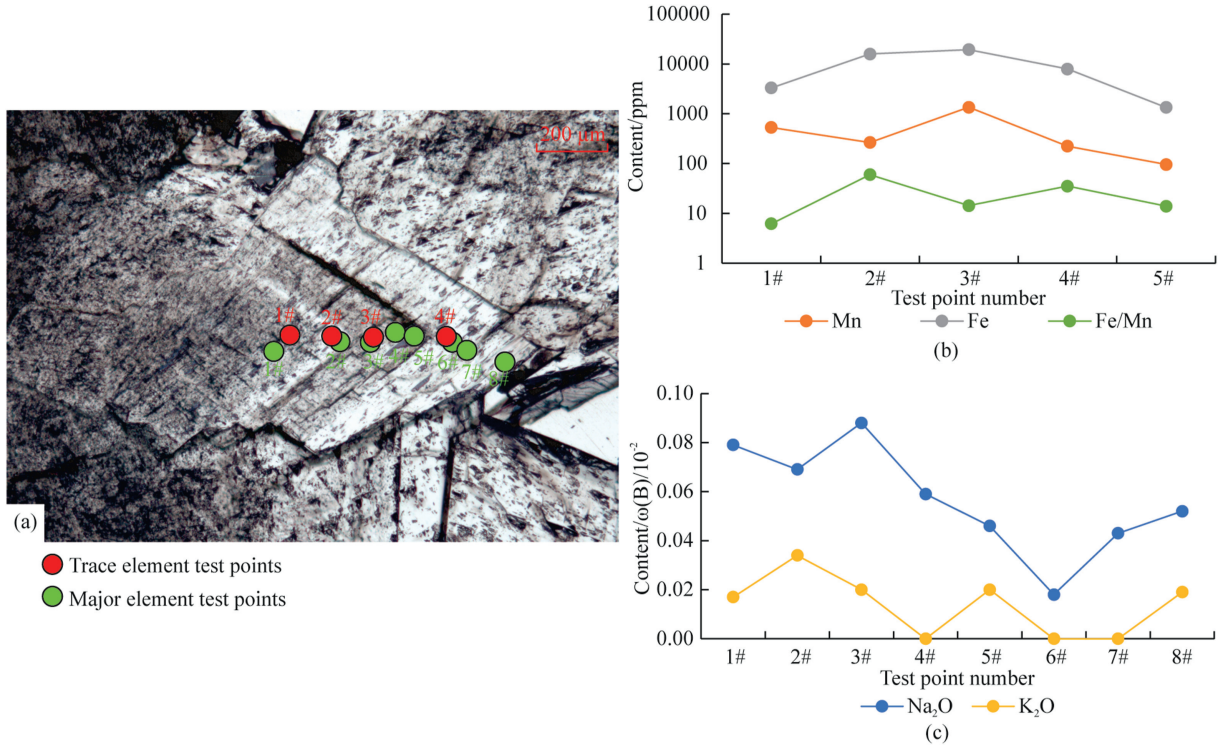

Fig. 8. Variation characteristics of major and trace elements in coarse crystalline dolomite of sample X5-2. (a) coarse crystalline dolomite filling dissolution pores, Xiweikou, Majiagou Formation, plane-polarized light (−); (b) line chart of trace element content at different positions; c. Line chart of major element content at different positions.

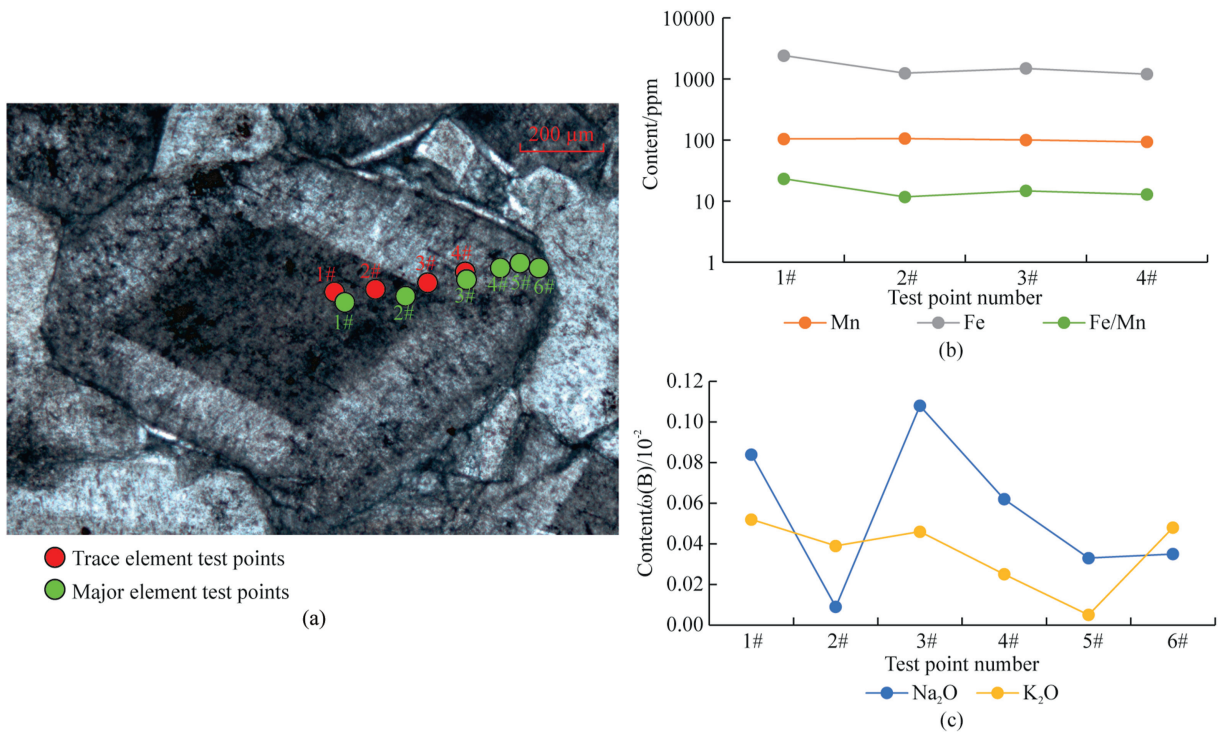

Fig. 9. Variation characteristics of major and trace elements in coarse crystalline dolomite of sample C07. (a) coarse crystalline dolomite with cloudy core-bright rim structure, Caojiagou, Yeli-Liangjiashan Formation, plane-polarized light (−); (b) line chart of trace element content at different positions; (c) line chart of major element content at different positions.

rocks generally have dark colors, predominantly euhedral to subhedral dolomite, with cloudy core-bright rim and zonal structures, and moderate to high dolomite ordering.

Sandy crystalline dolomites (fine, medium, and coarse crystalline) are associated with burial dolomitization. These rocks often exhibit a "sugary" texture, have dark colors, predominantly anhedral to subhedral dolomite, with cloudy core-bright rim, zonal, mottled, and aggregate structures, and the highest dolomite ordering. Compared to early-formed dolomites, they have more negative $\delta^{18}O$ values. Fluid inclusions have very high salinity and temperature (homogenization temperature usually greater than 50 °C). Additionally, burial dolomites are rich in Fe and Mn, and generally exhibit weak cathodoluminescence.

The high concentrations of Fe and Mn observed in these burial dolomites are particularly noteworthy. According to Cai et al. [57], the primary sources of Fe and Mn in such settings are deep fluids, especially during late-stage burial. These elements are mobilized through fluid activities and contribute significantly to diagenetic processes. Specifically, in low-sulfate environments, Mn and Fe oxides can drive anaerobic methane oxidation (AOM), leading to the precipitation of Fe- and Mn-rich minerals, as well as the formation of 13C-depleted calcite. This geochemical behavior is consistent with the characteristics observed in the sandy crystalline dolomites of the Ordos Basin, suggesting that the deep fluids not only provided the necessary ions but also played a key role in the diagenetic transformation of these dolomites.

The previous sections mainly analyzed the geochemical characteristics of micritic to finely crystalline dolomites and sandy crystalline dolomites in the Xiweikou, Jueshangu, and Caojiagou sections. The genesis parameters for these two types of dolomites are presented in Table 6.

Micritic to finely crystalline dolomites often coexist with gypsum and halite, and occasionally with pyrite aggregates. Their dolomite ordering is relatively low, averaging 0.726, indicating rapid dolomite growth, which leads to the disordered arrangement of $MgCO_3$ and $CaCO_3$ layers. Both $\delta^{13}C$ and $\delta^{18}O$ are negative, with an average $^{87}Sr/^{86}Sr$ value of 0.711402, higher than the global average $^{87}Sr/^{86}Sr$ of modern seawater (0.709073). Major and trace element analyses show that micritic to finely crystalline dolomites have high Na, K, and Sr, and low Fe and Mn, reflecting relatively high salinity during formation. For rare earth elements, both light and heavy rare earth elements are relatively enriched. Ce negative anomalies are not very pronounced, whereas Eu negative anomalies are evident, indicating a low-temperature alkaline environment. Some micritic to finely crystalline dolomites exhibit significant negative anomalies for both Ce and Eu, suggesting formation in a low-temperature, alkaline, weakly oxidizing environment, with left-leaning light REE and right-leaning heavy REE distribution patterns. Cathodoluminescence is generally rose-red to dark red. Combining petrographic and geochemical characteristics, micritic to finely crystalline dolomites likely formed during the penecontemporaneous period as products of penecontemporaneous dolomitization. The central ancient uplift influenced the study area, causing restricted seawater circulation during the Majiagou sedimentation period. The tidal flat environment, combined with the hot climate of the Majiagou period, led to increased seawater evaporation, salinity, and progressive penecontemporaneous dolomitization of sediments (Fig. 10a). Penecontemporaneous dolomitization occurs during the early stages after sedimentation, usually forming dolomite in shallow burial environments. These dolomites often have high porosity and permeability, with pore types mainly consisting of intergranular and intragranular pores, which is favorable for the formation of high-quality reservoirs. Additionally, the distribution of penecontemporaneous dolomite is often controlled by the original sedimentary facies belts, making the spatial distribution of reservoirs relatively predictable.

Sandy crystalline dolomites (fine, medium, and coarse crystalline) generally exhibit special structures such as "mottled," "cloudy core-bright rim," "zonal," and "aggregate" structures, and occasionally pyrite. Their dolomite ordering is generally high, averaging 0.848. Some samples have negative $\delta^{13}C$ and $\delta^{18}O$ values, and the average $^{87}Sr/^{86}Sr$ value is 0.710522, higher than the global average $^{87}Sr/^{86}Sr$ of modern seawater and slightly lower than that of micritic to finely crystalline dolomites. Sandy crystalline dolomites have low Na, K, and Sr, and high Fe and Mn, reflecting formation in a relatively closed diagenetic system. The high Fe and Mn concentrations observed in these dolomites are consistent with the findings of Cai et al. , which

Table 6
Genesis parameters of different types of dolomites.

Parameter		Micritic to finely crystalline dolomite	Sandy crystalline dolomite
Rock structure		Micritic structure, finely crystalline structure	Crystalline structure (fine-medium-coarse)
Crystal morphology		Euhedral to subhedral (finely crystalline dolomite)	Anhedral, subhedral, curved crystal faces
Accessory minerals		Gypsum, halite, pyrite	Pyrite
Ordering		0.571–0.867/0.726	0.667–1/0.848
Carbon and oxygen isotopes	$\delta^{13}C$ (‰)	−2.31~-0.85/-1.43	−2.62~2.05/-0.47
	$\delta^{18}O$ (‰)	−7.26~-5.13/-5.89	−6.87~-4.82/-6.16
Strontium isotopes	$^{87}Sr/^{86}Sr$	0.709503–0.715552/0.711402	0.709348–0.712553/0.710522
Major and trace elements	Na_2O (ppm)	0~6470/720	0~2160/510
	K_2O (ppm)	0~3530/520	0~2780/320
	Sr (ppm)	23.079–445.057/141.799	21.761–105.213/64.94
	Zn (ppm)	0.349–41.28/8.352	0.359–28.923/5.312
	Ba (ppm)	0.086–35.525/7.694	0.166–26.448/4.059
	Fe (ppm)	278.163–10237.084/1882.203	206.289–26652.837/6447.149
	Mn (ppm)	12.835–357.357/81.099	2.205–1352.904/228.878
	Characteristics	High Na, K, Sr, low Fe, Mn	Low Na, K, Sr, high Fe, Mn
Rare earth elements	ΣREE (ppm)	6.172–113.604/33.67	3.62–159.485/24.619
	ΣLREE (ppm)	5.498–78.918/29.053	2.967–153.61/22.505
	ΣHREE (ppm)	0.674–34.685/5.617	0.386–10.954/2.114
	ΣLREE/ΣHREE	0.887–13.356/6.968	2.792–26.148/8.214
	δCe	0.291–1.193/0.999	0.304–1.319/0.993
	δEu	0.459–1.078/0.853	0.574–1.268/0.844
	Distribution pattern	Left-leaning light REE, right-leaning heavy REE	Left-leaning light REE, right-leaning heavy REE
Cathodoluminescence		Rose-red to dark red light	Dark red to non-luminescent

Note: Test values are represented as minimum value–maximum value/average value.

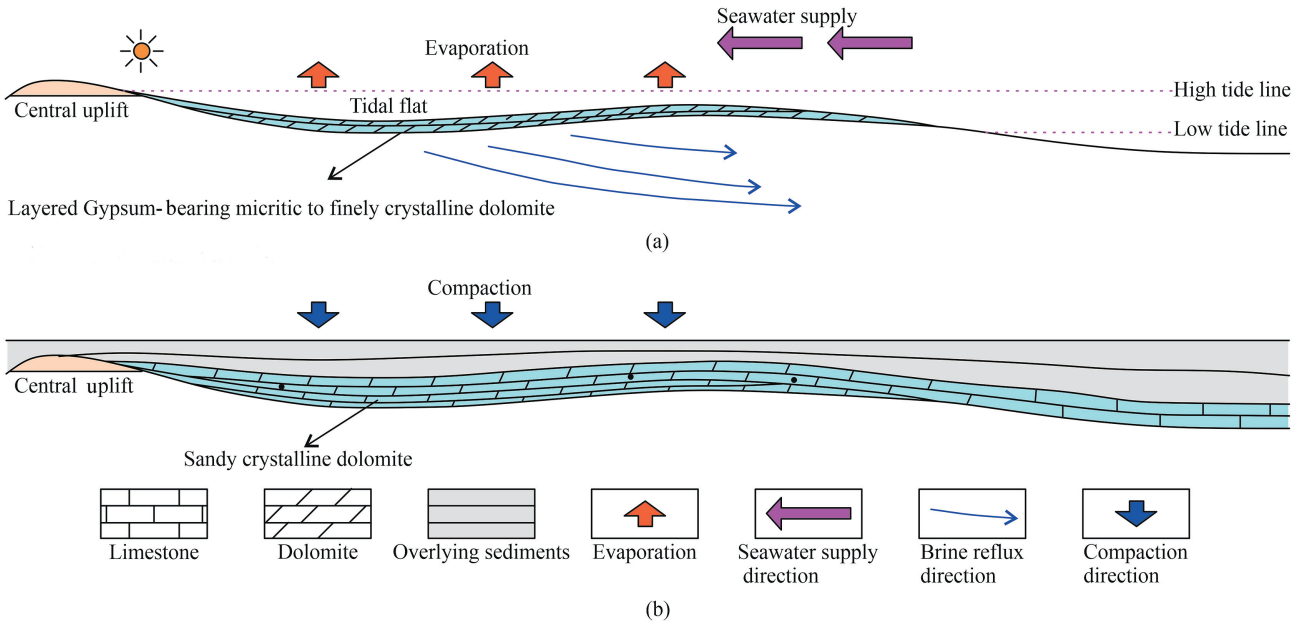

Fig. 10. Dolomite genesis models.

suggest that these elements were introduced by deep fluids during the late stages of burial. This process not only facilitated the recrystallization and growth of dolomite crystals but also contributed to the distinctive geochemical signatures observed in the sandy crystalline dolomites. The interaction between these deep fluids and the existing dolomites, under high-temperature and low-sulfate conditions, likely led to the incorporation of Fe and Mn into the dolomite structure, further supporting the burial dolomitization model as the dominant genesis mechanism in these strata. For rare earth elements, sandy crystalline dolomites lose light REE during late burial recrystallization, leading to greater depletion of heavy REE. Sandy crystalline dolomites show positive Eu anomalies and negative Ce anomalies, indicating formation in high-temperature oxidizing environments during late burial and compaction, with left-leaning light REE and right-leaning heavy REE distribution patterns. Cathodoluminescence is generally dark red to non-luminescent. Combining petrographic and geochemical characteristics, sandy crystalline dolomites likely formed during the burial stage. Their Mg^{2+} primarily originated from brines in the tidal flat environment, expelled laterally due to compaction [3]. After the Late Carboniferous, increased overlying sediments led to increased burial temperatures, causing continuous adjustment and recrystallization of previously formed micritic to finely crystalline dolomites and limestones, resulting in larger dolomite crystals as Fig. 10(b). Burial dolomitization occurs under deeper burial conditions and is mainly formed through fluid replacement processes. The porosity and permeability of burial dolomite may be affected by diagenetic processes such as compaction and cementation, leading to reduced petrophysical properties. However, burial dolomitization may be accompanied by dissolution processes that create secondary pores, improving reservoir quality. Since burial dolomitization is controlled by tectonics and fluid activities, predicting the distribution and quality of its reservoirs is relatively complex.

5. Conclusions

This study identified various types of dolomites in the Middle-Lower Ordovician strata along the southern margin of the Ordos Basin, including micritic dolomites, finely crystalline dolomites, and sandy crystalline dolomites. These types of dolomites exhibit significant differences in grain size, crystal morphology, and structure. Micritic and finely crystalline dolomites typically have smaller grain sizes and higher crystal euhedral degrees, while sandy crystalline dolomites display larger grains and lower euhedral degrees. These characteristics provide important clues for understanding the formation and development of dolomites in different diagenetic environments.

The study results show significant differences in dolomite ordering, geochemical composition, and cathodoluminescence features among different types of dolomites. Dolomite ordering reflects the degree of orderly arrangement of magnesium and calcium atoms during dolomite crystallization, which is usually related to diagenetic temperature and chemical environment during diagenesis. Geochemical analysis indicates that the distribution of rare earth elements, major and trace elements, and isotopic composition in dolomites can effectively indicate their diagenetic environment and processes. Cathodoluminescence analysis further reveals the distribution of trace elements (such as Mn and Fe) in dolomite crystals, providing additional evidence for understanding their diagenetic history.

Based on petrographic characteristics, geochemical data, and cathodoluminescence analysis, this study proposes the main genetic models for dolomites in the study area. The formation of dolomites mainly involves two stages: the penecontemporaneous stage and the burial stage. The formation of penecontemporaneous dolomites is related to high salinity and high pH in early seawater, usually occurring in relatively shallow marine environments. Burial dolomites, on the other hand, form in deep burial environments, with genesis closely related to burial depth, temperature, and fluid composition changes. These two genetic models not only determine the geochemical characteristics of dolomites but also affect their reservoir properties.

CRediT authorship contribution statement

Xinyi Tang: Formal analysis, Investigation, Methodology, Writing – original draft, Writing – review & editing. **Zijing Li:** Supervision, Methodology. **Hong Fang:** Resources, Data curation.

Yang Li: Writing – review & editing, Writing – original draft, Software, Resources, Methodology, Investigation, Formal analysis. **Zongyang Dai:** Supervision, Resources, Methodology, Investigation. **Tian Li:** Investigation. **Peng Lai:** Formal analysis, Data curation.

Declaration of competing interest

The authors declare that they have no known competing financial interests or personal relationships that could have appeared to influence the work reported in this paper.

References

[1] J. Warren, Dolomite: occurrence, evolution and economically important associations, Earth Sci. Rev. 52 (1) (2000) 1–81, https://doi.org/10.1016/S0012-8252(00)00022-2.

[2] A.H. Saller, N. Henderson, Distribution of porosity and permeability in platform dolomites: insight from the Permian of west Texas: reply, AAPG (Am. Assoc. Pet. Geol.) Bull. 85 (3) (2001) 530–532.

[3] Z.t. Su, The Study of Dolomite Genesis and Diagenisis System of Majiagou Formation Aroud Paleo-uplift,Ordos, Chengdu University of Technology, 2011.

[4] W. Zhao, A. Shen, Z. Qiao, L. Pan, A. Hu, J. Zhang, Genetic types and distinguished characteristics of dolomite and the origin of dolomite reservoirs, Petrol. Explor. Dev. 45 (6) (2018) 983–997, https://doi.org/10.1016/S1876-3804(18)30103-4.

[5] Z.c. Ding, G. Xing, D. Guo dong, T. Jin, H. Jiang tao, W. Shao yi, Z. Zhen yu, W. Hui, Characteristics, genesis and distribution of the Ordovician pre-salt dolomite reservoirs in Ordos Basin, Marine Origin Petroleum Geology 26 (1) (2021) 16–24.

[6] Y. Wang, Z. Shi, H. Qing, Y. Tian, X. Gong, Petrological characteristics, geochemical characteristics, and dolomite model of the lower cambrian Longwangmiao Formation in the periphery of the Sichuan Basin, China, J. Petrol. Sci. Eng. 202 (2021) 108432, https://doi.org/10.1016/j.petrol.2021.108432.

[7] Z.t. Su, S. Wei, L. Hui hong, H. Sun long, L. Guo qing, M. Hui, Research progress and development trend of the genesis of dolomite reservoirs, Nat. Gas Geosci. (2022) 1–20.

[8] L. Wen, J. Zhang, L. Pan, H. Ma, Z. Li, W. Li, W. Xie, Z. Wang, X. Fu, Y. Wang, R. Li, Characteristics, controlling factors and exploration prospects of microbial dolomite reservoirs in the second member of Dengying Formation, Penglai-Zhongjiang area of central Sichuan Basin, Petroleum Geology & Experiment 45 (5) (2023) 982–993, https://doi.org/10.11781/sysydz202305982.

[9] D.D. Dolomieu, Lettre du Commandeur Deodat de Dolomieu a M. Picot de la Peyrouse: Sur un genre de Pierres calcaires très-peu effervescentes avec les Acides et phosphorescentes par la collision, Malta, 30.01. 1791, observations et mémoires sur la physique, sur l'histoire naturelle, et sur les arts et métiers 39 (1971) 3–10.

[10] J.R. Allan, W.D. Wiggins, Dolomite reservoirs, Geochemical techniques for evaluating origin and distribution: AAPG Contin. Educ. Course Note Ser. 36 (1993) 129.

[11] B.H. Purser, A. Brown, D.M. Aissaoui, D. Zenger, M.T.B. Purser, Nature, Origin and Evolution of Porosity in Dolomites, International Association of Sedimentologists, Special Publication, 1994.

[12] Y. Wang, Dolomite problem and precambrian enigma, Adv. Earth Sci. 21 (8) (2006) 857.

[13] J.A. McKenzie, C. Vasconcelos, Dolomite Mountains and the origin of the dolomite rock of which they mainly consist: historical developments and new perspectives, Sedimentology 56 (1) (2009) 205–219.

[14] C. Li, S.-X. Pan, H.-B. Wang, J.-X. Deng, J.-G. Zhao, Z. Li, Y. Zhang, Rock physical characteristics of deep dolomite under complex geological conditions: a case study of 4th member of Sinian Dengying Formation in the Sichuan Basin, Pet. Sci. (2024), https://doi.org/10.1016/j.petsci.2024.03.015.

[15] D. Liu, T. Chen, Z. Dai, D. Papineau, X. Qiu, H. Wang, K. Benzerara, A non-classical crystallization mechanism of microbially-induced disordered dolomite, Geochem. Cosmochim. Acta (2024), https://doi.org/10.1016/j.gca.2024.05.005.

[16] J.E. Adams, M.L. Rhodes, Dolomitization by seepage refluxion, AAPG Bull. 44 (12) (1960) 1912–1920.

[17] K. Badiozamani, The dorag dolomitization model, application to the middle Ordovician of Wisconsin, J. Sediment. Res. 43 (4) (1973) 965–984.

[18] B.W. Mattes, E.W. Mountjoy, Burial Dolomitization of the Upper Devonian Miette Buildup, Jasper National Park, Alberta, 1980.

[19] J.A. McKenzie, K.J. Hsü, J.F. Schneider, Movement of Subsurface Waters under the Sabkha Abu Dhabi, UAE, and its Relation to Evaporative Dolomite Genesis, 1980.

[20] G.R. Davies, L.B. Smith Jr., Structurally controlled hydrothermal dolomite reservoir facies: an overview, AAPG Bull. 90 (11) (2006) 1641–1690.

[21] K. Spangenberg, Die künstliche Darstellung des Dolomits, Z. Kristallogr. Cryst. Mater. (2015), https://doi.org/10.1524/zkri.1913.52.1.529.

[22] W.z. Zhao, S. An jiang, Q. Zhan feng, P. Li yin, H. An ping, Z. Jie, Genetic types and distinguished characteristics of dolomite and the origin of dolomite reservoirs, Petrol. Explor. Dev. 45 (6) (2018) 923–935.

[23] Y. Bai, W. Liu, W. Xu, Dolomite genesis and dolomitization mechanisms of the ordovician lower yingshan formation, Gucheng area, Tarim Basin, China, J. Petrol. Sci. Eng. 215 (2022) 110570, https://doi.org/10.1016/j.petrol.2022.110570.

[24] M. Yang, C. Liu, W. Yang, D. Zhu, Y. Yu, F. Chen, H. Zou, Characteristics and genesis of thick layer dolomites in the lower cambrian Xixiangchi Group, eastern Sichuan Basin, Fault-Block Oil Gas Field 31 (4) (2024) 599–610.

[25] S.y. Fu, Formation Mechanism and Dolomitization of Pre-salt reservoir:The Ordovician Majiagou Fifth Formation, East – Central Ordos Basin 10.26986/d.cnki.gcdlc.2019.001107, Chengdu University of Technology, 2019.

[26] C.y. Yu, J.p. Cui, Geochemical characteristics and genesis of dolomite in Majiagou Ma55 submember of the Northeast Yishan slope, Ordos Basin, Earth Sci. 44 (8) (2019) 2761–2774.

[27] Y. Han, F. Si yi, C. Hong de, S. Zhong tang, Z. Jun xing, Z. Cheng gong, H. Lin jun, Geochemical characteristics and genetic model of Ordovician Ma-4 Member dolomite in central eastern Ordos Basin, China, J Chengdu Univ Technol (Science & Technology Edition 49 (1) (2022) 70–83.

[28] L. Feng, H. Yang, L. Li, L. Peng, G. Yang, X. Wang, Characteristics and genetic mechanism of dolomites of lower cambrian Xiaoerbulake formation in Tarim Basin, Fault-Block Oil Gas Field 31 (5) (2024) 827–835.

[29] W.w. Zhao, B.q. Wang, Geochemical characteristics of dolomite from 5th member of the Ordovician Majiagou Formation in Sulige area,Ordos Basin, cta Geoscientica Sinica 32 (6) (2011) 681–690.

[30] Z.l. Huang, W. Chun ying, M. Zhan rong, R. Jun feng, B. Hong ping, Sedimentary sequence of ordovician Majiagou Formation in central and eastern part of Ordos Basin and its control over reservoir development, China Petroleum Exploration 20 (5) (2015) 20–29.

[31] H.p. Bao, Y. Fan, C. Zheng hong, W. Qian ping, W. Chun ying, Origin and reservoir characteristics of ordovician dolostones in the Ordos Basin, Nat. Gas. Ind. 37 (1) (2017) 32–45.

[32] Z. Shou kang, L. Ling, T. Xiu cheng, S. Jian, W. Li chao, H. Dao jun, H. Yun dong, D. Shao feng, B. Hong ping, Study on the genesis and diagenesis of medium-coarse crystal dolomite of the Member 5 of Majiagou Formation in the central-eastern Ordos Basin, China, Journal of Chengdu University of Technology(Science & Technology Edition 47 (6) (2020) 691–710.

[33] J. Zeng, S. Dong, Origin of dolomite in middle permian qixia formation in northwestern Sichuan Basin: a case study of chejiaba section, Petroleum Geology & Experiment 46 (2) (2024) 288–298, https://doi.org/10.11781/sysydz202402288.

[34] L. Marheni, M. Alsuwaidi, S. Morad, A. Koeshidayatullah, A. Herlambang, B. Al Muhairy, K. Al Tameemi, Links between anhydrite precipitation and dolomitization during cycles of sea level change: insights from the late jurassic arab formation, Abu Dhabi, United Arab Emirates, Mar. Petrol. Geol. 170 (2024) 107106, https://doi.org/10.1016/j.marpetgeo.2024.107106.

[35] R.A. Ali, Dolomitization mechanism of Pila Spi formation (middle- late eocene) in the high folded zone, Northern Iraq, Kuwait J Sci 50 (2) (2023) 105–114, https://doi.org/10.1016/j.kjs.2023.02.015.

[36] H. Jiang, J. Liang, K. Azmy, J. Cao, L. Wen, G. Zhou, Y. He, S. Liu, F. Huo, H. Wen, Controls of sedimentary facies and sealevel fluctuation on dolomitization: the lower cambrian Longwangmiao Formation in Sichuan Basin, China, Mar. Petrol. Geol. 157 (2023) 106465, https://doi.org/10.1016/j.marpetgeo.2023.106465.

[37] Y. Li, X. Yang, X. Wang, C. Fan, X. Fan, Y. Zhang, R. Yang, Y. Li, Z. Huang, F. Huo, Multistage dolomitization influenced by the Emeishan large igneous province: petrographical and geochemical evidence, Mar. Petrol. Geol. 164 (2024) 106780, https://doi.org/10.1016/j.marpetgeo.2024.106780.

[38] S. Fu, C. Zhang, A. Chen, A.J. Van Loon, J. Zhao, Z. Su, H. Chen, Chapter 3 - origin and evolution of dolomite reservoirs in the ordovician Majiagou Formation, central and eastern Ordos Basin, NW China, in: R. Yang, A.J. Van Loon (Eds.), The Ordos Basin, Elsevier, 2022, pp. 49–67.

[39] F. Li, X. Ma, X. Lai, Petrography, geochemistry and genesis of dolomites in the upper Cambrian Sanshanzi Formation of the western Ordos Basin, northern China, J. Asian Earth Sci. 223 (2022) 104980, https://doi.org/10.1016/j.jseaes.2021.104980.

[40] L. Feng jie, D. Ling chun, Z. Jun xing, L. Yue gang, X. Fang, L. Fu ping, Dolomite genesis in member Ma55 of Majiagou Formation,sudong area,Ordos Basin, Acta Pet. Sin. 37 (3) (2016) 328–338.

[41] X.y. Yang, Origin of Dolomite and Controlling Factor of Dolomite Reservoir in Ma55 Sub-member of Ordovician Majiagou Formation in Ordos Basin, Chengdu University of Technology, 2018.

[42] Z. Su, A. Chen, A.J. van Loon, S. Yang, C. Zhang, S. Xu, Chapter 4 - depositional model and diagenetic evolution of hydrocarbon reservoirs in deep dolomites of the Ordos Basin, China, in: R. Yang, A.J. Van Loon (Eds.), The Ordos Basin, Elsevier, 2022, pp. 69–89.

[43] J. Zhou, Z. Yu, D. Wu, J. Ren, D. Zhang, S. Wang, C. Yin, Y. Liu, Restoration of formation processes of dolomite reservoirs based on laser U-Pb dating: a case study of Ordovician Majiagou Formation, Ordos Basin, NW China, Petrol. Explor. Dev. 49 (2) (2022) 327–338, https://doi.org/10.1016/S1876-3804(22)60027-2.

[44] S. Zhong, X. Tan, G. Hu, W. Nie, M. Yang, D. Zhang, J. Zheng, J. Xu, G. Dong, D. Xiao, Z. Lu, Control of paleogeographic pattern on sedimentary differentiation of evaporite-carbonate symbiotic system: a case study of the sixth sub-

member of Ordovician Majiagou Formation M5 Member in central-eastern Ordos Basin, NW China, Petrol. Explor. Dev. 49 (4) (2022) 837–850, https://doi.org/10.1016/S1876-3804(22)60314-8.
[45] B. Ding, H. Liu, D. Xu, L. Qiu, Z. Zhang, Genetic model of tabular orebody in Nalinggou uranium deposit, Ordos Basin: constraint from clay minerals studies, Ore Geol. Rev. 165 (2024) 105844, https://doi.org/10.1016/j.oregeorev.2023.105844.
[46] Q. Kong, L. Kong, J. Yao, J. Ren, K. Wu, T. Zhao, Sources and exploration potential of Ordovician subsalt natural gas in Ordos Basin, China, J. Nat. Geosci. 9 (6) (2024) 401–416, https://doi.org/10.1016/j.jnggs.2024.11.001.
[47] S. Zhong, X. Tan, L. Wei, J. Xu, Q. Wang, Y. Xiong, C. Wu, J. Du, Tectono-sedimentary evolution and oil-gas geological significance of first to third member of Ordovician Majiagou Formation in Ordos Basin, NW China, Petrol. Explor. Dev. 51 (5) (2024) 1202–1216, https://doi.org/10.1016/S1876-3804(25)60535-0.
[48] Z.w. Hu, Dolomitization of the Triassic Feixianguan Formation, Northeastern Sichuan Basin, Chengdu University of Technology, 2010.
[49] N. Liu, The Study of Dolomite Reservoir Genesis in Longwangmiao Formation of Lower Cambrian in Central and Southren Sichuan Basin, Chengdu University of Technology, 2015.
[50] L. Jiang, C. Cai, R.H. Worden, S.F. Crowley, L. Jia, K. Zhang, I.J.J.S. Duncan, Multiphase dolomitization of deeply buried Cambrian petroleum reservoirs, Tarim Basin, North-west China 63 (7) (2016) 2130–2157.
[51] Y. Hu, C. Cai, D. Liu, C.L. Pederson, L. Jiang, A. Shen, A.J.S. Immenhauser, Formation, diagenesis and palaeoenvironmental significance of upper Ediacaran fibrous dolomite cements 67 (2) (2020) 1161–1187.
[52] Y. Hu, C. Cai, C.L. Pederson, D. Liu, L. Jiang, X. He, S. Shi, A.J.P.R. Immenhauser, Dolomitization History and Porosity Evolution of a Giant, Deeply Buried Ediacaran Gas Field (Sichuan Basin, China), vol. 338, 2020 105595.
[53] D. Liu, C. Cai, Y. Hu, Y. Peng, L.J.M. Jiang, P. Geology, Multistage dolomitization and formation of ultra-deep lower cambrian Longwangmiao Formation reservoir in central Sichuan Basin, China (Q. Forecast Rep.) 123 (2021) 104752.
[54] B. Jiu, W. Huang, Y. Li, The effect of hydrothermal fluids on Ordovician carbonate rocks, southern Ordos Basin, China, Ore Geol. Rev. 126 (2020) 103803, https://doi.org/10.1016/j.oregeorev.2020.103803.
[55] Y. Du, T. Fan, H.G. Machel, Z. Gao, Genesis of upper cambrian-lower ordovician dolomites in the Tahe Oilfield, Tarim Basin, NW China: several limitations from petrology, geochemistry, and fluid inclusions, Mar. Petrol. Geol. 91 (2018) 43–70, https://doi.org/10.1016/j.marpetgeo.2017.12.023.
[56] H. Zheng, F. Lu, Y. Dong, B. Liu, X. Zhang, K. Shi, J. He, H. Qing, Magma-driven thermal convection dolomitization of the Lower-Middle Ordovician strata caused by Mg sourced from underlying Cambrian dolomites in the Tarim Basin, China, Mar. Petrol. Geol. 163 (2024) 106740, https://doi.org/10.1016/j.marpetgeo.2024.106740.
[57] C. Cai, D. Liu, Y. Hu, T. Huang, Z. Jiang, C. Xu, Interlinked marine cycles of methane, manganese, and sulfate in the post-Marinoan Doushantuo cap dolostone, Geochimica et Cosmochimica Acta 346 (2023) 245–258.